COMPUTATIONAL FLUID DYNAMIC AND HEAT TRANSFER MODELING OF STIRLING ENGINE

BY

AHMED SALIH HAMZA ABUELYAMEN

A Thesis Presented to the
DEANSHIP OF GRADUATE STUDIES

KING FAHD UNIVERSITY OF PETROLEUM & MINERALS

DHAHRAN, SAUDI ARABIA

In Partial Fulfillment of the
Requirements for the Degree of

MASTER OF SCIENCE

In

MECHANICAL ENGINEERING

December 2016

KING FAHD UNIVERSITY OF PETROLEUM & MINERALS

DHAHRAN- 31261, SAUDI ARABIA

DEANSHIP OF GRADUATE STUDIES

This thesis, written by **AHMED SALIH HAMZA ABUELYAMEN** under the direction of his thesis advisor and approved by his thesis committee, has been presented and accepted by the Dean of Graduate Studies, in partial fulfillment of the requirements for the degree of **MASTER OF SCIENCE IN MECHANICAL ENGINEERING.**

Dr. Habib Abualhamayel
(Advisor)

Dr. Zuhair M. A. Qasem
Department Chairman

Dr. Rached Ben-Mansour
(Member)

Dr. Salam A. Zummo
Dean of Graduate Studies

Dr. Fahad Al-Sulaiman
(Member)

23/1/17
Date

© Ahmed Salih Hamza Abuelyamen

2016

Dedication

This humble effort is dedicated to my loving

Parents

For their endless love, support and encouragement

ACKNOWLEDGMENTS

I would like to acknowledge KFUPM and the mechanical engineering department for this opportunity and the unlimited knowledge I benefited from during my time here. I also extend my thanks and appreciation to Dr. Rached Ben-Mansour for his enormous contribution to this work, support, encouragement and guidance. Also, I would like to thank Dr. Habib Abualhamayel and Dr. Fahad Al-Sulaiman for their support. My thanks also go to my colleagues, friends and the Sudanese community at KFUPM.

TABLE OF CONTENTS

ACKNOWLEDGMENTS ..... **V**

TABLE OF CONTENTS ..... **VI**

LIST OF TABLES ..... **IX**

LIST OF FIGURES ..... **X**

LIST OF ABBREVIATIONS ..... **XII**

NOMENCLATURE ..... **XIII**

ABSTRACT ..... **XV**

ملخص الرسالة ..... **XVII**

CHAPTER 1 INTRODUCTION **1**

1.1 Operating Principle of Stirling Engine **2**

1.2 Applications of Stirling Engine **3**

1.3 Stirling Engine Configurations and Driving Mechanisms **4**

1.4 Design Methods of Stirling Engine **6**

1.4.1 Zero-order Analysis **6**

1.4.2 First-order Analysis **6**

1.4.3 Second-order Analysis **7**

1.4.4 Third-order analysis **7**

1.4.5 Multi-dimension Analysis (CFD analysis) **7**

1.5 Motivation and Significance of the study **7**

1.6 Research Objectives **8**

CHAPTER 2 LITERATURE REVIEW 9

CHAPTER 3 MATHEMATICAL FORMULATION 28

3.1 Problem Formulation 28

3.2 Parametric Study of β-type Stirling Engine 31

3.3 Radiative Heat Transfer Implementation 33

3.4 Heater and Cooler Shapes Optimization 36

3.5 Piston Motion Mechanisms Investigation 37

3.6 Stirling engine Configurations Study 40

3.7 Numerical Procedure 43

CHAPTER 4 RESULTS AND DISCUSSION 45

4.1 Dynamic-mesh Validation 45

4.2 Parametric Study of β-type Stirling Engine 49

4.2.1 Effect of Initial Charge Pressure 49

4.2.2 Effect of Heater Temperature (TH) 59

4.2.3 Effect of Shifting Temperature Limits (TH & TC) 61

4.3 Impact of Radiative Heat transfer on β-type Stirling Engine 64

4.4 Heater and Cooler Shapes Optimization 67

4.5 Piston Motion Mechanisms investigation 70

4.6 Stirling Engine Configuration Study 75

CHAPTER 5 CONCLUSIONS & RECOMMENDATIONS 78

5.1 Conclusions 78

5.2 Recommendations and Future Work 80

REFERENCES 81

VITAE **85**

LIST OF TABLES

Table 2.1 Setup summary of CFD literature review 26
Table 2.2 Main results of summary of CFD literature review 27
Table 3.1. Dimensions of the β-type Stirling engine in (mm). 28
Table 3.2 Dimension parameters used in crank-shaft and scotch mechanisms. 39
Table 3.3 Geometry dimensions for α, β, and γ-types of Stirling engine (mm). 41
Table 4.1 Coefficients of efficiency fit curve equation 3.22 54
Table 4.2 Coefficient of generated power fit curve equation 3.23. 54
Table 4.3 Comparison of indicated power at different temperature limits. 63
Table 4.4 Comparison of radiative model impact on Stirling engine performance. 67
Table 4.5 Performance of Stirling engine with different fin shapes. 67
Table 4.6 Engine performance under different piston motion mechanisms. 75
Table 4.7 Engine performance for different Stirling engine configurations. 76

LIST OF FIGURES

Figure 1.1 Global consumption of energy [1]..... 2
Figure 1.2 Stirling engine operation cycle: (a) expansion, (b) regeneration cooling fluid, (c) compression, and (d) regeneration heating fluid [2]. 3
Figure 1.3 Solar mirror focused on Stirling engine by Stirling Energy Systems, Inc [2]... 4
Figure 1.4 Stirling engine for PC cooling [2]. 4
Figure 1.5 Stirling engine configurations [3]..... 5
Figure 3.1 β-type Stirling Engine 29
Figure 3.2 Different Heater/Cooler fins profile shapes. 37
Figure 3.3 Stirling engine motion mechanisms; (a) Rhombic, (b) Crankshaft, and (c) Scotch mechanism. 38
Figure 3.4 Stirling engine configurations; (a) Alpha, (b) Beta, and (c) Gamma types.... 41
Figure 4.1 A comparison of adiabatic compression process done by CFD and analytical thermodynamic model. 46
Figure 4.2 Computational meshed domain of beta-type Stirling engine. 47
Figure 4.3 P-V diagrams of expansion and compression zones comparing between the present work and Salazar and Chen's work [45]. 48
Figure 4.4 β-type Stirling engine performance at different charge pressure and temperature limits of 300-800 K for air gas..... 50
Figure 4.5 β-type Stirling engine performance at different charge pressure and temperature limits of 300-800 K for He gas. 52
Figure 4.6 β-type Stirling engine performance at different charge pressure and temperature limits of 300-800 K for H2 gas. 53
Figure 4.7 Temperature contours inside β-type Stirling engine using H_2 gas at 4 bar charge pressure and temperature limits of 300-800 K. 56
Figure 4.8 Temperature contours and velocity vectors at expansion chamber at various steps for H_2 gas at 4 bar and temperature limits of 300-800 K. 57
Figure 4.9 Heat transfer at top and bottom of the cylinder for the case of H_2 gas at 1 bar charge pressure and temperature limits of 300-800 K. 57
Figure 4.10 Error in the power output due to taking average pressure at each chamber separately. 59
Figure 4.11 Effects of T_H on Stirling engine performance at 1 bar charged pressure and T_C of 300 K; (a) work output and (b) efficiency. 60
Figure 4.12 Effect of shifting operational temperature range on β-type Stirling engine performance at 1 bar charge pressure; (a) work output and (b) efficiency. .. 63
Figure 4.13 Radiation effect on heat transfer profile of β-type Stirling engine..... 66
Figure 4.14 Average temperature profiles on the expansion chamber for different fins shapes. 68
Figure 4.15 Average pressure profile for different fin shapes. 69
Figure 4.16 Heat transfer profiles for different piston motion mechanisms. 71

Figure 4.17 Volume change of rhombic mechanism. 73
Figure 4.18 Positon and direction of the piston and displacer during one cycle for the rhombic mechanism. 74
Figure 4.19 Pressure profile for different piston motion mechanisms..... 74
Figure 4.20 Temperature contours for the alpha-type Stirling engine. 76
Figure 4.21 Heat transfer profiles in (a) narrow connecting pipe (b) total surface area... 77

LIST OF ABBREVIATIONS

BDC	:	Bottom Dead Center
CFD	:	Computational Fluid Dynamics
DO	:	Discrete Order
NSD	:	Normalized Separation Distance
RTE	:	Radiative Heat Transfer
S2S	:	Surface to Surface
TDC	:	Top Dead Center

NOMENCLATURE

a, b, c, d	Constants
c_p	Specific heat at constant pressure (kJ.kg^{-1}.K^{-1})
g	Gravity acceleration (m.s^{-2})
k	Thermal conductivity (W.m^{-1}.K^{-1})
l_1, l_2, l_3, l_4	lengths of the linkages of the rhombic drive mechanism (m)
l_d	Height of displacer (m)
n	Normal direction to a plane.
p	Pressure (Pa or bar)
q	Heat flux (W.m^{-2})
r_1, r_2	Radius of displacer and cylinder (m)
t	Time (s)
u, v	Velocity components in x- and r-direction (m.s^{-1})
$\tilde{u}, \tilde{v}$	Relative velocity in x- and r-direction (m.s^{-1})
u_c, v_c	Moving frame velocity components in x- and r-direction (m.s^{-1})
u_p, u_d	Piston and displacer velocities (m.s^{-1})
x, r	Cylindrical coordinates in x- and r-direction
G	Regenerative channel gap (m)
L	Distance between two gears (m)
L_{dt}	Length from the linkage l_4 to top surface of the displacer (m)
L_{pt}	Height from the linkage l_1 to top surface of the piston (m)
L_t	Height of the engine (m)
Q_{in}, Q_{out}	Heat absorb and rejected from the Stirling engine (W)
Q_i	Total heat transfer during step i (W)
R	Gas constant (J.kg^{-1}.K^{-1})
R_d	Offset distance from the crank to the center of gear (m)
T, T_C, T_H	Temperature, cold-end temperature, and hot-end temperature (K)
V	Volume (m^3)
W_{out}	Power output (W)

Greek Symbols

δ	Solid wall thickness (cylinder wall) (m)
η	Thermal efficiency (%)
μ	Viscosity ($kg.m^{-1}.s^{-1}$)
θ	Crank angle (degree or radian)
ρ	Density ($kg.m^{-3}$)
ω	Rotational speed ($rad.s^{-1}$)

Subscripts

f	Fluid

ABSTRACT

Full Name : Ahmed Salih Hamza Abuelyamen

Thesis Title : Computational Fluid Dynamic and Heat Transfer Modeling of Stirling Engine

Major Field : Mechanical Engineering

Date of Degree : December 2016

High demand for energy along with the sustainable rise in air pollution lead the efforts of looking for a new reliable technology for power generation. Stirling engine technology is a promising solution for energy production because it can use any source of heat to generate power. For instance, Stirling engine can be combined with a solar dish so it is useful for countries which are rich with solar energy.

In this work, a numerical modeling for Stirling engine was performed using computational fluid dynamics (CFD) to help in understanding its characteristics by combining flow field and heat transfer field. The study included radiative heat transfer, which has been ignored in CFD works on Stirling engine. The engine consists of three main heat exchangers: heater, cooler and regenerator. Because most of the work done in the literature focus on investigating and optimizing of the regenerator, this study concerns with an optimization of the heater and the cooler. The investigation was carried out for different operation conditions such as operating pressure and heater temperature. In addition, a comparison between the performance of the three main types of Stirling engine (alpha, beta and gamma) were studied. Moreover, different piston motion mechanisms (rhombic, crankshaft, and scotch) were examined also.

It turns out that the optimum operational condition depends on the type of the working fluid. For instance, for the beta-type Stirling engine under temperature limits of 300-800 K the optimum charge pressures are 1.75, 2.5 and 10 bar for air, He and H_2 respectively. Additionally, among the three Stirling engine types with the proposed geometry and boundary conditions, the Stirling engine of alpha-type with annular connecting pipe reflects the best performance in term of power output (9.96 W) and thermal efficiency (10.08%). Furthermore, for beta-type Stirling engine running with atmospheric air charge pressure and temperature limits of 300-800 K, rhombic motion mechanism has the highest power output (9.61 W) and thermal efficiency (8.3%) compared to the crankshaft and scotch mechanisms. Moreover, it was shown that neglecting radiative heat transfer leads to 13% error in the estimation of heat transfer values and 18% error in the generated power output, which emphasize the importance of implementing the radiation model in the Stirling engine analysis. In order to attach a fin to the main engine body, it should have a shape that allows gasses to be circulated and well mixed with each other. Otherwise, the fin results in a negative impact due to its dead volume.

ملخص الرسالة

الاسم الكامل: أحمد صالح حمزه ابواليمن

عنوان الرسالة: نمذجة حركة تحسيب الموائع وانتقال الحرارة للمحرك ستيرلنغ

التخصص: الهندسة الميكانيكية

تاريخ الدرجة العلمية: ديسمبر 2016

إن الطلب المتزايد للطاقة بالإضافة الى الإرتفاع المستمر لمعدل تلوث الهواء أدى للبحث عن طرق جديد يمكن الإعتماد عليها لإنتاج الطاقة. محرك استيرلنغ يعتبر من أحد هذه الحلول الواعدة لإنتاج الطاقة، وذلك لإمكانية استخدامه لاي نوع من أنواع مصادر الطاقة الحرارية وتحويلها الى طاقة حركية يمكن الإستفادة منها. فمثلاً يمكن ان تُوظف الطاقة الشمسية لتشغيل محرك استيرلنغ وبهذا فإن هذا المحرك يكون ذو فائدة عظيمة للبلدان الغنية بالطاقة الشمسية.

تهدف هذه الدراسة الى النمذجة الرياضية لمحرك استيرلنغ بإستخدام حركة تحسيب الموائع ، وذلك سيؤدي للمساعدة في فهم خصائص السريان عن طريق ربط كل من حركة الموائع وانتقال الطاقة الحرارية. تم تضمين انتقال الحرارة بالإشعاع في هذا البحث رغم ان كل البحوث الأُخرى المتعلقة بمحرك استيرلنغ تم تجاهل هذا النوع فيها من انتقال الحرارة. يتكون هذا المحرك من ثلاثة أجزاء رئيسية هي: السخان، المبرد، ومسترجع الحرارة. معظم البحوث المتعلقة بمحرك استيرلنغ تتحدث حول تحسين كفاءة المسترجع الحرارية، ولم يجد كل من السخان والمبرد حظهما الوافر من تلك البحوث، لذلك في هذا البحث تم التركيز على تحسين أداء السخان والمبرد. بالإضافة الى ذلك فإن البحث سوف يمتد ليحدد أفضل عوامل تشغيلية لمحرك استيرلنغ. هذه العوامل التشغيلية هي عبارة عن درجة الحرارة وضغط الشحن للمحرك. كما أنه سيتم مقارنة أداء الأنواع الثلاثة الرئيسية للمحرك ستيرلنغ وهي ("ألفا"، "بيتا"، "قاما"). أيضا سيتم دراسة ثلاثة أنواع مختلفة من الحركة تستخدم لتحريك المكبس في الحرك وهي ("رومبك"، عمود المرفق، "سكوتش").

من خلال هذا البحث اتضح ان افضل نقطة تشغيلية لمحرك استيرلنغ تعتمد على نوع مائع التشغيل المستخدم. على سبيل المثال، عندما يعمل محرك ستيرلنغ من النوع "بيتا" بين درجتي حرارة تبريد وتسخين بين الثلاثمئة والثمانيمئة درجة مطلقة فإن أفضل أداء للمحرك يكون عند ضغط 1.75 بار وذلك عندما يُستخدم الهواء كمائع لتشغيل المحرك، ولغاز الهيليوم فإن أفضل ضغط هو 2.5 بار، أما لغاز الهيدروجين فإن أفضل ضغط تشغيلي هو 10 بار. وأيضا من بين الأنواع الثلاثة للمحرك ستيرلنغ فإنه تم توضيح أن أكبر طاقة مولدة تم انتاجها كانت عن طريق النوع "الفا" ذو الاسطوانة الحلقة للربط بين منطقة التسخين والتبريد ومقدارها هو 9.6 واط وكذلك سجل هذا النوع أفضل كفاء حرارية (10.08%) من بين الأنواع الثلاثة لنفس الظروف التشغيلية. أما من حيث نوع الحركة المستخدمة لتحرك المكبس فأن نوع الحركة "رومبك" قد سجل أفضل أداء من حيث الطاقة المتولدة 9.61 واط وكذلك من حيث الكفاءة الحرارية 8.3%، حيث تمت المقارنة مع نوع الحركة ذات عمود المرفق ونوع الحركة المسماة "سكوتش". وقد تم ذلك للمحرك ستيرلنغ ذو النوع "بيتا" الذي يعمل بالهواء عند الضغط الجوي ودرجات حرارة تشغيلية بين 300-800 درجة مطلقة. بالإضافة الى ذلك فقد بينت هذا الدراسة أن عدم تضمين الطاقة الإشعاعية عند تقييم أداء المحرك يؤدي الى خطأ بمقدار 13% في تقدير الطاقة الحرارية المنتقلة من والى المحرك وهذا الخطأ يرتفع الى 18% عند حساب القدرة المولدة من المحرك ستيرلنغ؛ لذلك من المهم جدا تضمين الطاقة الإشعاعية عند عملية تقييم أداء المحرك ستيرلنغ. وكذلك من الأمور المهمة التي ناقشها هذا البحث هي عملية إضافة الزعانف للمحرك. حيث كشفت هذه الدراسة أن هذه الزعانف يجب ان تكون بهيئة تسمح للغازات داخل المحرك أن تنتشر وتختلط ببعضها البعض بصورة جيدة، وإلا فإن ذلك سيؤدي الى تأثير سلبي على أداء المحرك نسبة لزيادة حجم المحرك الناتجة عن وجود الزعانف.

CHAPTER 1

INTRODUCTION

The global energy consumption increasing tremendously while there is gradually depletion of non-renewable energy resources. Figure 1.1 represents the global energy consumption for different energy sources [1]. For instance, a huge amount of coal and liquids fuels are burnt in order to generate electricity. The combustion of these fossil fuels produces a tremendous amount of pollutions like nitrous oxides (NO_x), sulfurous oxides (SO_x) and particulate matter (PM). Accordingly, the needed for green energy is highly important.

Stirling engine is one of the most promising innovations that will help in solving the energy crisis. It attracts researchers in industry and academic fields, due to its interesting characteristics. It is classified as an external combustion engine. It can utilize various types of heat resources like Sun energy or waste heat energy. In addition, it has a quiet operation with a low level of noise. More important future of Stirling engine is its possibility of operating in absence of oxygen.

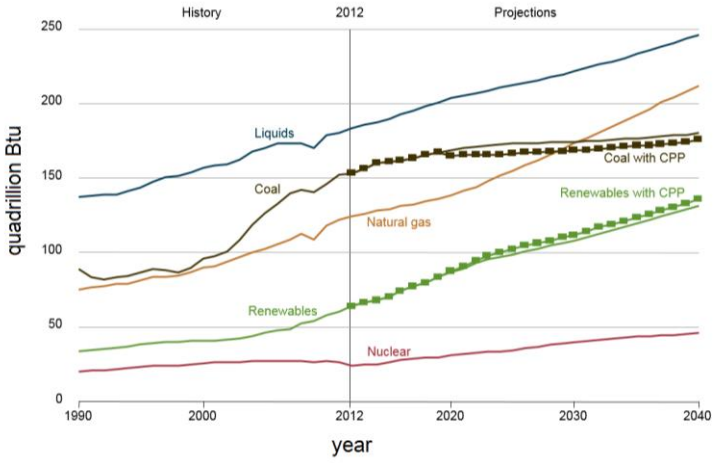

Figure 1.1 Global consumption of energy [1]

1.1 Operating Principle of Stirling Engine

The operation principle of Stirling engine is based on the fact that when a gas is heated at closed system its pressure will increase, therefore it pushes a piston producing work.

The engine composed of hot space, cold space, regenerator and connected pipes as show in Figure 1.2. It is operating at a close cycle so there is no gas enters or exits from the cylinders. The Figure also demonstrates the four processes of operation. The first process is an expansion (Figure 1.2a) in which most of the fluid in the system exists in the hot chamber. Due to the heat supply, the gas expands driving the two pistons towards the bottom dead center (BDC). The power produced stores in the flywheel to complete the cycle. After that the piston of hot space starts to move toward the top dead center (TDC) pushing the gas from the hot space to the cold space through the regenerator which absorbs heat from gas so it reaches cold space with relatively low temperature (Figure 1.2b). This process called regeneration process. The third process is compression. In which both pistons move toward TDC compressing the working fluid (Figure 1.2c). It can be noticed, in the compression process, most of the fluid exists in cold space resulting in less power

consumed during compression. In the final process (Figure 1.2d), gas in cold side is pushed through the regenerator, hence its temperature rises again when it reach the hot zone and starts a new cycle.

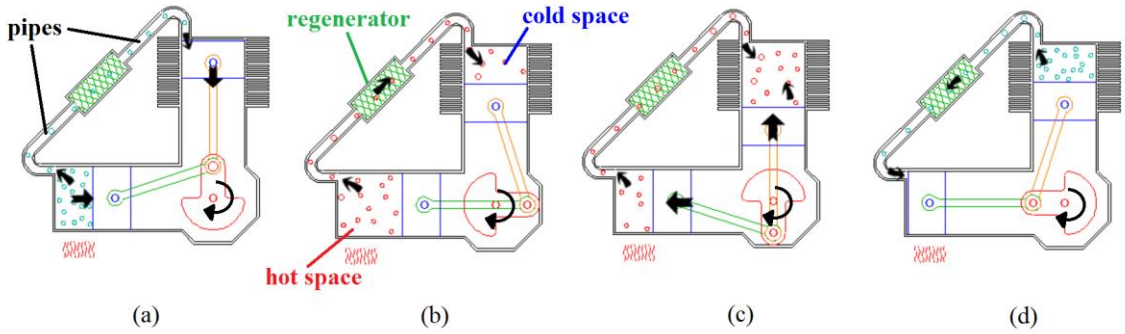

Figure 1.2 Stirling engine operation cycle: (a) expansion, (b) regeneration cooling fluid, (c) compression, and (d) regeneration heating fluid [2].

1.2 Applications of Stirling Engine

One of the characters that make Stirling engine differ from others, its ability to employ a various type of heat sources for instance solar energy, geothermal heat, industrial waste heat and even heat from fossil fuel combustion. When solar energy is utilized the system will be environmentally friendly so no more carbon dioxide would produce. The most common application is utilizing solar parabolic mirror focused on the hot chamber in Stirling engine (Figure 1.3). In general Stirling engine used to produce electricity. In addition, due to the sensitivity of Stirling engine to low temperature differences it can be used for cooling PC chips [2] (Figure 1.4). Motherboard maker MSI (Taiwan) used Stirling engine for the processor. They claimed it converts 70% of heat energy to power to drive the fan. In the 1970s, Ford develops a vehicle running in Stirling engine, but unfortunately, it required about 20 seconds after ignition to start moving. Furthermore, when Stirling cycle is reversed it can be used as refrigeration cycle to produce Stirling cryocoolers. The first

Stirling cycle cryocooler was developed in the 1950s at Philip and commercialized for liquid nitrogen productions [2].

Figure 1.3 Solar mirror focused on Stirling engine by Stirling Energy Systems, Inc [2]**.**

Figure 1.4 Stirling engine for PC cooling [2]**.**

1.3 Stirling Engine Configurations and Driving Mechanisms

Stirling engines are commonly found in three basic configurations: alpha, beta, and gamma. Each of the main configurations has unique advantages and disadvantages due to their variation in geometry and arrangement.

Alpha configuration consists of two separate cylinders (Figure 1.5a). They connected to each other by a connecting pipe, usually filled by regenerator. Each cylinder has a sealed piston. One of these cylinders is heated, while the other is subjected to cooling. The second type of Stirling engine is Beta-type. It has only one cylinder contains the two pistons (Figure 1.5b). One of them is sealed (it called the power piston) while the other piston is utilized to displace the working fluid between cold and hot chamber (and it called displacer piston). The two pistons are mounted concentrically within the same cylinder, as a result, it required a driver rod from displacer extending through power piston. Moreover, beta-type may have some problem with cooling since it occurs at the same cylinder just beneath heating section. On the other hand, γ-type is much the same to the β-type except that cooling chamber is extended to a new cylinder (Figure 1.5c).

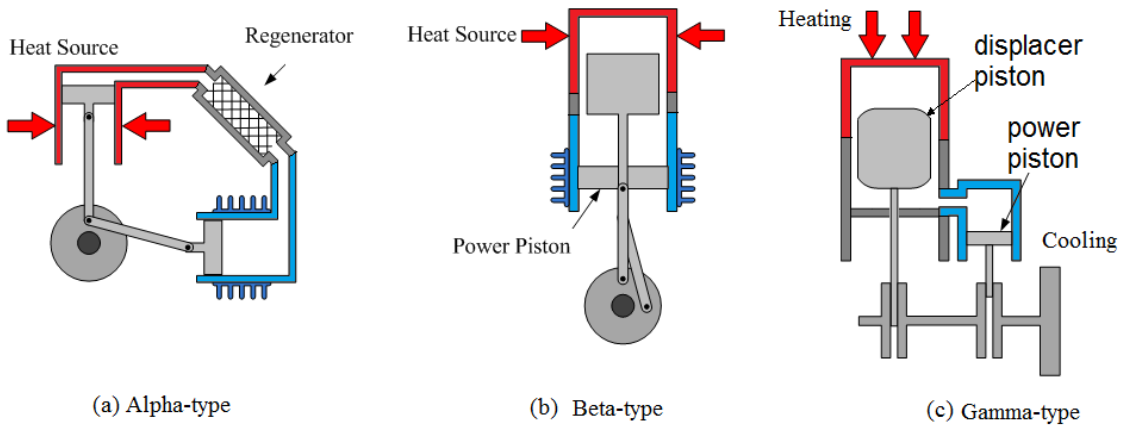

Figure 1.5 Stirling engine configurations [3].

All the Stirling engine types can utilize a crankshaft driver mechanism, however, there are various mechanisms can be used for instance Youk-driver, Rhombic driver, Ross driver, lever controller, Scotch-crank and free-piston motion. These mechanisms controlling how

does the engine volume vary during the cycle so they arrange the existence of the gas to be in cold zone during the compression stroke and in the hot zone during the expansion stroke.

1.4 Design Methods of Stirling Engine

There are four methods that used to design and predict the performance of Stirling engine: zero-order analysis, first-order analysis, second-order analysis, third-order analysis (or nodal design method) and fourth order analysis (or CFD simulation)[4], [5]. The term order here has no things to do with the mathematical error, but it is kind of classification according to complexity as the order increase.

1.4.1 Zero-order Analysis

This model is the simplest such as generalized Beale number derived by William Beale. It assumes that most of the engines work under similar conditions. It allows for quick estimation of the power output depending on the engine size, but it is not very useful for detailed design and optimization of Stirling engine.

1.4.2 First-order Analysis

This analysis is established firstly by Schmidt in which the power output is obtained by considering isothermal hot and cold spaces. The volume is assumed to have a sinusoidal function. All heat enter the cycle takes place in the expansion space, while all heat rejected from the cycle takes place in the compression space. In addition, a perfect regenerator is utilized and there is no axial heat conduction. There are no losses taking into account, so usually a correction factor is applied.

1.4.3 Second-order Analysis

In these model, a set of simplified system is solved by balancing the equations to identify the output power and thermal efficiency. It assumes adiabatic compression and expansion in cold and hot regions respectively. In the second-order analysis, the power losses such as friction and gas leakage are taken into account. Also, it considers heat losses which include wall conduction, imperfect heat transfer in regenerator and displacer shuttle losses. However, all these losses are decoupled (i.e. do not depend on each other).

1.4.4 Third-order analysis

The third-order analysis is also known as nodal analysis. It divides Stirling engine into a network of nodes. Then, one-dimensional differential equations for conservation of mass, energy and momentum are solved in addition to the equation of state. These differential equations are solved numerically.

1.4.5 Multi-dimension Analysis (CFD analysis)

In computational fluid dynamics (CFD) the heat transfer and fluid mechanics are solved simultaneously. It explains properties distributions inside the engine, for instance, a value of heat transfer coefficient is varied wildly across the engine the things that do not take into account in the third-order analysis. It provides more details inside the engine, so it results in better understanding of the actual heat transfer and flow features within the engine.

1.5 Motivation and Significance of the study

Recently, renewable energy and energy efficiency have become more critical areas of research. Stirling engine is one of the most promising innovation that is expecting to

help in solving the energy problems. It is classified as an external combustion engine, so it can utilize any source of heating such as Sun energy or waste heat energy. Theoretically, the thermal efficiency of Stirling engine is same as Carnot cycle efficiency. However, practically the thermal efficiency is small. Hence, this research is aiming to improve the performance of Stirling engine through different methods. Thus, Stirling engine can be commercialized for thermal energy generation applications by combined it with solar energy and waste heat energy.

1.6 Research Objectives

The overall objective of this study is to investigate numerically the performance of the Stirling engine taking into account all modes of heat transfer including radiation heat transfer which has not been accounted for in most of the published studies. Accordingly, the specific objectives of this study are:

- To develop a dynamic model that incorporates the flow and heat transfer in Stirling engine.
- Carry out a parametric study to optimize the various heater and cooler shapes.
- Study the effects of different piston motion mechanisms.
- Make a comparison of the performance of the three common configurations of Stirling engine (Alpha, Beta, and Gamma).

CHAPTER 2

LITERATURE REVIEW

An experimental study of crankshaft mechanism of γ-type Stirling engine was carried out by Cinar and Karabulut [6]. The engine has a 276 cc swept volume with two expansion cylinders and one displacer. I was heated at the top part of the cylinder and cooled by water at the bottom. They tested two types of working fluid which are air and helium. The experiment was performed for a different range of temperature between 700 and 1000 ˚C via an electrical furnace. In addition, various charge pressure was conducted to optimize the engine performance. The maximum power obtained was about 128 W. They concluded that the power output when helium gas was utilized almost double that obtained from the air at same operation conditions. Also, they presented that the optimum pressure depends on the source temperature and the engine start to vibrate after this optimum value.

Yucesu et al. [7] built and examine a β-type Stirling engine. They studied the performance of the engine at different source temperature experimentally by utilizing an electrical heater. They used atmospheric air as working fluid. The engine was driven by a crank shaft mechanism and used cooling water system. Only 5.98 W was obtained as maximum power from the engine testing at 208 rpm and a hot source temperature of 1000 ˚C. They concluded that the performance of engine (speed, power, and torque) was improved by increasing the heat source temperature.

Karabulut et al. [8] conducted a nodal analysis for a Stirling engine had a power cylinder situated inside the displacer cylinder. The cylinder had a slotted groove that

increases the surface area. They used FORTRAN program to run the analysis for 103 cells constitute the engine volume. In order to calculate the temperature variation, they used first law of thermodynamics while the change in engine volume was computed from the dynamic of the crankshaft mechanism. Furthermore, they obtained convective heat transfer coefficient by assuming the flow on the slot surfaces were fully laminar and developed. They studied the effect of different working fluid mass and different regenerator areas and came to the conclusion, the rate of heat exchange in the heater is proportional to the regenerator area and it keeps improving with regenerator surface until a value where a further increase of the surface wouldn't be useful. In addition, they showed that there was an optimum working fluid mass after it the work per cycle tends to decrease.

Furthermore, An experimental investigation on flow and heat transfer in the heater head region of free-piston Stirling engine was presented by Jiang and Simon[9]. The engine used helium as working fluid with an operation temperature of 888 K. In order to characterize the flow, they measured the velocity and temperature profiles at seven locations in the head of the heater. Their results show a remarkably low value of average heat transfer coefficient due to the thick boundary layer and separation zones on the head inner wall.

A numerical simulation of Gamma-type Stirling Engine was performed by K. Mahkamov[10] to prior manufactured prototype. The engine was already designed using first-order model and the power expected was far less than actually obtained power. Mahkamov employed both second-order model and 3D CFD model to identify factors restricting the power output. The CFD model used k-e turbulent model for a compressible flow. The investigation showed that there are two major factors limiting the power output which are the hydraulic losses in the regenerator and the large value of the dead volume.

Consequently, he modified the prototype by eliminating some of the dead volumes through converting Stirling engine configuration from γ-type to α-type. Furthermore, he calibrated his models against experimental data obtained on 0.5 kW_e Stirling engine and found that the second-order predicts the indicated power output with nearly 30% accuracy while this value decrease to 12-18% for CFD model.

Wongwises and Kongtragool [11] investigated the performance of γ-type Stirling engine experimentally. The engine worked at ambient pressure and it used air as working fluid. They tested the engine with four different solar intensities. The power generated from the engine was small (maximum 1.69 W) and it is proportional to solar intensity.

Iskander Tlili et al. studied a solar power system based on the Stirling dish technology[12]. They applied their model which included energy losses and pressure loss in the heater, cooler and regenerator of α-type Stirling engine worked with a Hydrogen. On the design process, they optimize values of various temperature, rotational speed and dead volume for the best performance. Their engine was driven by Yoke Ross mechanism. They came to the result that there was an optimal swept volume before and after this optimum volume the power decreases. In addition, they showed that a dead volume has a great impact on limiting the power output. Furthermore, they concluded that the small porosity results in high pressure drop due to increases of friction factor, however, their results indicated that small porosity will produce high thermal efficiency.

In addition, they showed in a developed work [13], due to optimal design parameters the efficiency could be improved by 20%.

Moreover, they conducted a numerical simulation model to explore physical parameters and geometrical shapes that influent the performance of Stirling engine[14]. They tested their model to an experimental data for a prototype of GPU-3 Stirling engine manufactured by General Motor. It used a rhombic mechanism for motion and utilized helium as working fluid. It had a power of about 4 kW and thermal efficiency of 35% under the conditions of operation temperature between 288K and 977 K, mean pressure of 4.13 MPa, and 41.72 Hz. The power and the thermal efficiency got from the modeling were 4.27kW and 39.5%, respectively. Their model is an adiabatic second-order that taking into account the thermal losses while mechanical frictional losses didn't considered. To validate their model, they compared it with those achieved by Urieli and Berchowitz for GPU-3 at similar conditions. They pointed out that the energy losses result from conduction in the cooler and the heater could be neglected, while it was considerably in the regenerator (35% of total losses). Furthermore, they showed that losses coming from shuttle effect, external conduction in the regeneration, and dissipation by the pressure drops in the regeneration were also significant. Moreover, they made an optimization for the engine performance included the volume, thermal conductivity, and porosity of the regenerator as well as the influence of the fluid mass, expansion volume, and piston conductivity.

Scollo et al. [15] designed and constructed a prototype of α-type Stirling engine that using Helium as working fluid. To perform the preliminary design they used the code from Urieli which utilized Schmidt analysis. They found that the temperature stabilized after about half an hour.

Batmaz and Üstün [16] designed and manufactured a α-type Stirling engine that used a Helium for its operation. It had two cylinder heaters and it was driven by a crankshaft

mechanism. They used a simulation software developed by Karabulut for the design of the engine. They assumed that the hot cylinder and cold cylinder were at their sources temperature and the working fluid was ideal gas without any leakage of the Helium. They tested the engine within temperature range 650-1000 ˚C using an electrical heater and pressure from atmospheric pressure up to 2 MPa. One of the main results was that the engine speed increases linearly with the heater temperature. Furthermore, the gap distance between the displacer and its cylinder played a great role in effective heat transfer. As it narrow, it enhances the heat transfer however the pumping work would increase. They designed the engine to had 500 W, nevertheless, only 118 W was obtained.

Parlak et al. [17] modified Urieli and Berchowitz's model for the gamma-type Stirling engine. To make the model more reasonable they added several losses so they considered the pressure drop due to friction and heat losses. They divided the engine to five volumes and applied the conservation law of mass and energy. Then they developed a FORTRAN code in order to get the solution of governing equations.

Karabulut et al. [18] studied the performance of β-type Stirling engine from thermodynamics and kinematic point of view. They analyzed a different range of convective heat transfer coefficient and various values of clearance for several piston lengths using isothermal analysis. Also, they examined three type of mechanisms which are crank mechanism, rhombic mechanism, and lever controller drive mechanism. Lever controller mechanism produced the highest dead volume, nevertheless, its work was greater than crank mechanism due to better cooling and heating at constant volume. They found that the work output increases proportionally with the heat transfer coefficient. They validated their work against an experimental work and it showed good accuracy at low

speed, but at high speed the accuracy decrease due to the viscous losses, mechanical friction losses and a small amount of heat transfer between solid and fluid zones which were not accounted in the theoretical analysis.

Karabulut et al. [19] designed and built a β-configuration Stirling engine with lever controller to arrange the movement of the displacer piston. They designed the Stirling engine to work at low heat temperature (200 ˚C). In order to enhance the heat transfer, they made slots in the inner surface of the cylinder which increases the surface area. They tested their Stirling engine with air as working fluid for several charge pressure up to 4.6 bars and constant temperature for the hot and cold side. They got maximum power output around 52 W at ~ 450 rpm and 2.8 bars and this value increased by 50% after augmenting the inner surface of the displace by slots.

Karabulut et al. [20] perform an experimental study of β-type Stirling engine with helium working fluid. The engine had a lever mechanism that drove the displacer. It heated by burning a liquefied petroleum gas. The test was conducted with operation condition temperature range of 180-260 ˚C and charge pressure of 1-4.5 bars. They noticed that as hot source temperature increases, the engine endurance of external load increase and it could run at rather low speeds. Also, they concluded that there was an optimum charged pressure. Furthermore, they obtained only 52W as maximum power when the air was utilized. It is too small compared to that maximum power which was obtained by helium 183 W at 600 rpm, 260 ºC, and 4 bars.

Cheng and Yu [21] developed a numerical model for estimating the thermodynamic performance of a β-type Stirling engine. The engine used air for operating and it utilized a

rhombic mechanism for pistons dynamics. They solved the energy equation for the control volumes by considering the effects of the regenerator, non-isothermal condition, and head cylinder heating thermal resistance. Besides, they assumed that the flow in the regenerative channel was incompressible and fully developed. Moreover, viscous shear in the regenerative channel was considered so it results in the pressure difference between the cold and hot chambers. They performed a parametric study to show the impact of heat source temperature, the distance between two driving gears of rhombic mechanism, and gap size between displacer and the inner diameter of the cylinder. They pointed out that the power output increases proportionally with the source temperature and with increases of an offset distance from the crank to the center of the gear. On contrary, the generated power and the efficiency decrease as the distance between the two gears increases. Furthermore, they found there an optimal gap size of the regenerator leads to high regenerative effectiveness and low friction shear losses.

Eid et al. [22] conducted an experimental investigation on the effect of elbow-bend geometry. They studied the influence of tube arrangement on the performance of heat exchangers which were used as cooler and heater in the α-type Stirling engine. They presented the effect of three shapes of elbow geometry with three different tubes bank arrangement. They found that the tubes bank arrangement through an elbow-bend had an absolutely huge influence on the pressure drop. Furthermore, they developed correlations for the effectiveness of the heat exchanger, friction factor, and Nusselt number from the studied geometry. They recommended that they could be used for the design of α-type Stirling engine.

Puech and Tishkova [23] provided a theoretical investigation on the performance of Stirling engine. Their study included a sinusoidal motion the pistons as well as a hypothetical discontinuous linear motion. They used an isothermal model for predicting thermal efficiency and the output power. They studied the effects of imperfect regeneration and dead volume. The main results of their analysis showed that by utilizing a regenerator has 100% of effectiveness the Carnot efficiency could be obtained regardless of the dead volume.

Another work done by Cheng and Yu [24] was performing a dynamic model of β-type Stirling engine which uses cam-drive motion. Then they coupled it with a thermodynamic model. So that the instantaneous rotation speed was predicted from the equation of rotation motion after evaluating the torque exerted by the flywheel, pressure, the mass of inertia, friction force, and the external load. The gas pressure was evaluated from the thermodynamic model while an empirical correlation for the friction force was used. They presented that the all different initial rotation speed that was tested leads to the same final cycle-average rotation speed after a period of time (i.e. when the engine reaches to stabilized condition). Also, they added there was an optimum value of moment inertia of flywheel that results in maximum power output. Furthermore, they investigated the effects of initial pressure in the chamber, heat source temperature, regenerator gap size, and the phase angle. They found that there was an optimum phase angle for high cycle-average rotation speed and another optimum value for high cycle-average output power and thermal efficiency.

Moreover, they conducted more study for the same engine but with rhombic drive mechanism [25] using the same principles. They found that all different initial rotational

speed and moment of inertia leads to the same final cycle rotational speed as same as happened with the cam-driven mechanism. However, the large moment of inertia results in low fluctuation in the engine speed.

Cheng and Yang [26] carried out a theoretical analysis for three type of Stirling engine; α-, β-, and γ-type. They optimized the swept volume ratio and the phase angle. They accomplished their investigation by introducing a number of dimensionless variables and assuming that the hydraulic pressure drop was negligible so the pressure was uniform through the engine. They came to conclusion; the β-type Stirling engine generated the highest power output and γ-type was the lowest one. Also, they recommended that α-type was not suitable for low temperature operation will γ-type was most capable of work at low temperature.

Chen et al. [27] developed a numerical analysis on a γ-type Stirling engine with double power pistons. The engine charged with helium. They modified Chen and Yu's model to include more engine losses and they assumed that the thermal resistances at the wall of the compression and expansion chambers were changing according to the change of the surface area, while Chen and Yu's model assumed it to be constant. They validated their code against the original one of Chen and Yu's model by setting the heat transfer and friction losses to be zero as well as the effect of conjugate heat transfer because Chen and Yu did not take them into account. Their parametric study showed that the regeneration effectiveness introduces a distinguished effect of the thermal efficiency. Furthermore, they showed that the power piston crank radius and the initial pressure had an influence on the power output.

Ibrahim[28] developed a 2D-axisymmertic CFD model to simulate the experimental test rig done by Jiang and Simon[9]. The original experimental geometry (3D) had radially oriented slots in the heater so, it cannot simulate as 2D-axisymmetric. However, by using same hydraulic diameter he found good results agreement further away from the heater. He showed that most of the pressure drop occur in the regenerator at 90 and 270 C.A. where the piston and flow had the highest velocity. His result showed errors in the heat transfer coefficient fluctuating between 23% and 75%.

Costa et al. [29] studied numerically the pressure drop in 3D wound woven wire matrix for Stirling engine. They selected air as working fluid and it was assumed to be incompressible and viscous. All fluid thermal properties were assumed to be constant. The second order Up Wind scheme was selected to discretize the continuity and momentum equations. They studied two various regenerators; stacked wire and wound woven wire matrix. Each one was studied with two various layouts; totally aligned and misaligned. In addition, they studied the effect of porosity in all cases. Furthermore, they used laminar model for stacked woven wire matrix where ($Re > 175$) and for wound woven wire matrix ($Re > 230$). On the other hand, they utilized RNG k-ε model for turbulent flow. They derived a correlation to estimate pressure drop friction factor for stacked woven wire. They evaluated the obtained correlation against experimental oscillating flow done by Tanaka et al. and Gedeon and Wood. They included the wire mesh diameter in the correlation as well as Re because it showed effects on the friction factor. After that, they extended their work to drive a correlation for pressure drop friction factor in a wound wire woven. It also depended on the wire diameter and Reynolds number range up to 400. The study covered diameter range 0.08 to 0.11 mm and porosity range from 0.472 to 0.638.

Another investigation of compact porous-sheets heat exchanger is accomplished by Li et al. [30]. They run a 3D simulation for α-type Stirling engine which was driven by Ross mechanisms. The engine is charged with Helium at atmospheric pressure. They utilized Fluent 14 for the numerical simulation with PISO scheme for pressure-velocity coupling. They came to the conclusion that in the comparison between the conventional wire mesh regenerator and the porous sheet regenerator, the late has the lowest entropy generation rate which results in high thermal efficiency and high power output.

Araoz et al. [31] presented a model that can be adopted for different Stirling engine types (alpha, beta, and gamma). The model considered an adiabatic working spaces with isothermal heat exchanger and it included the dead volumes and imperfect regeneration. They estimated the power and the efficiency then it compared to numerical and experimental data of GPU-3 Stirling engine reported by the NASA Lewis Research Center. It reflects an error of brake power (±4%) and (±5%) for the brake efficiency and these values increase to ±15% in high frequencies and low pressures operating conditions.

Bouvenot et al. [32] developed a dynamic model for simulating a micro combined heat and power devices (μCHP). It based on the empirical expressions plus an energy balance on the device for different input and output parameters.

Chen et al. [33] developed a compressible CFD code to study the characteristics of heat transfer for 3D γ-type Stirling Engine driven with the crankshaft mechanism. Their Stirling model geometry consists of two power pistons. Their studies accomplished for very simple geometry without a regenerator for purpose of simplifications. Furthermore, they simulate only quarter of the geometry due to symmetry on two faces. Their results

included; Temperature distribution, velocity vectors, the amount of heat input and output from the engine, and the power output. They found differences between their results and those obtained by the second order method especially in the rates of heat transfer. The term ‘order’ here has no things to do with the mathematical error, but it is kind of classification according to complexity as the order increase. Moreover, they discover a highly non-uniform temperature distribution within the engine during the cycle which reflects an inaccuracy of some of the one-dimensional models. The power obtained from this model was very small (about 0.6 W) due to the absence of the regenerator and low operating temperature difference range (300-400 K).

Alfarawi et al. [34] adopted an ideal adiabatic model in order to estimate the performance of β-type Stirling Engine thermodynamically. It utilized an exhaust heat gasses as source heat for the Stirling engine which used to drive the alternator. Besides, they carried out a CFD investigation to optimize the geometry of the heater and the cooler. The ideal thermal efficiency was found to be 40% with a power of 1.5 to 2 kWe.

Another numerical and experimental study of Stirling engine regenerator conducted by Tutar et al. [35]. They studied the pressure drop losses in wound woven wire matrix regenerator. The tested a porosity range between 52% and 72% and Reynolds number (Re) ranging from 5 to 50 in a laminar flow regime and came up with a correlation related the friction coefficient factor with Re.

Furthermore, Costa et al. [36] developed a thermal non-equilibrium porous media model for Stirling engine. Its accuracy was validated with a detailed numerical 3D woven wire matrices. They claimed that without the need for experimental work, their model can

predict the coefficients of porous media. They found that the stacked configuration has better overall performance compared to a wound woven wire matrices.

Paul and Engeda [37] developed an ideal adiabatic and simple heat exchanger model. Their model expects the engine power beside the specific fuel consumption with an error of ±14%. They used a log men-temperature difference to model the external heat transfer. They compared the results with an experimental data of the GPU-3 Stirling engine. GPU-3 is a β-type Stirling engine which has a rhombic mechanism. It uses a tube bundle heater to heat the working fluid.

Hosseinzade and Sayyaadi [38] modeled a hybrid of adiabatic and finite speed thermodynamics analysis to simulate and optimize a Stirling engine. Their model included pressure drop in heaters and regenerator, also it deals with mechanical friction losses on the piston side. Their analysis recorded a high percentage of error in estimating thermal efficiency (+14.9%), indicated power (+33.6%) and brake power (+69.7%).

Chen et al [39] investigated the impacts of moving regenerator on the performance of a rhombic driven β-type Stirling Engine. They treated the moving regenerator as a porous medium. They studied the effect of different values of porosity and discovered that despite the fact that the pressure loss is proportional with the porosity, however as the porosity was increased the overall engine performance was improved in term of net power output and thermal efficiency.

One of leader CFD simulation of Stirling engine was carried out by k. Mahkamov and Ingham [40],[41]. They investigated the performance of complex geometry of an alpha-type Stirling Engine in order to gain more insight into the heat transfer processes

within Stirling engine. The model was simplified as 2D with axis-symmetry. They adopted the standard k-ε turbulence model for compressible flow. Their results show that the change of working gas temperature in different planes along the axis of the compression space is different from results obtained by second-order analysis. On other words, it is non-harmonic in time. In contrast, temperature profiles for expansion space and regenerator were similar to second-order analysis. Furthermore, in a second-order analysis, the power output was found to be double the value obtained by CFD analysis. But unfortunately, they did not validate their model.

NASA also pay attention for developing and improving Stirling engine performance. One of the most fasted simulations of the whole Stirling engine was performed by Dyson et al.[42]. They simulated a free-piston configuration of Stirling engine using axisymmetric. They claimed that their model simulates a complete engine cycle with fully converged in less than an hour. They demonstrated that by careful grid design to reduce computational effort and by utilizing parallel computers with fast communication hardware. A comparison of their results with Sage (its 1D code) reflects an over-predicting in indicated power. Nevertheless, further comparison with an actual performance data shows that the axisymmetric simulation is more accurate than Saga results. It worth to mention that they set the boundary condition for the cold-end temperature in their simulation lower by about 14˚C than temperature value in actual data. This because experiment there might be some losses and it needs to be overcome by increasing source temperature little bit. The results reflected the amount of net heat in, heat out and work out in the simulation study and experimental data are almost the same with thermal efficiency around 32%. Moreover, they provided helpful tips on grid design

especially in problems related to solution convergence and stability. Furthermore, they utilized a segregated implicit solver but later they found coupled implicit solver leads to a good result. In addition, they reported that Cleveland State University suggested to obtain the steady-state firstly will be a good initial condition for a transient solution.

Lin et al. [43] conducted simulation analysis of 3D free-piston Stirling engine which used a helium as working fluid. Unfortunately, their results in terms of heat added to the cycle do not match the experimental data. The CFD model reflected a high amount of heat input compare to experimental data. Furthermore, according to their operating conditions the Carnot efficiency is about 62% while they only obtained an efficiency of 28.5% and the experiment showed the efficiency of 33%.

Costa et al. [44] studied heat transfer in 3D wound woven wire matrix of a Stirling engine regenerator. Firstly they developed a 3D model for stack woven and validated the obtained correlation of heat transfer coefficient against empirical relationship of Tanaka et al. [6] and Gedeon and Wood's work. After that, they extended the model for wound woven wire matrices. The fluid was assumed to be viscous, incompressible and Newtonian with constant flow properties. In addition, their study covered Reynolds number range from 4 to 400, a wire diameter of 0.008 to 0.11 mm and volumetric porosity range from 0.6 to 0.68. They consider the flow to be laminar in low Re range and turbulent at higher Re range. The results of Nu correlation for stack woven showed good agreement with empirical correlation proposed by Gedeon and Wood especially for Re greater than 40, while it was not fit well with the correlation proposed by Tanaka et al. Furthermore, their results reflected a value of Nu number lower by 20% for wound woven matrices compared to stack woven matrices for $20 < Re < 400$. Moreover, they did not notice a significant

influence of volumetric porosity in Nu due to the small selected value of volumetric porosity (0.6-0.68). Therefore they suggested to study it in further investigation.

Salazar and Chen [45] investigated the characteristics of rhombic-drive beta-configuration Stirling engine working with air as working fluid. The problem was treated as axisymmetric laminar and thermal properties along with the viscosity are assumed to be constant. They adopted a scheme of pressure-velocity coupling in Lebon et al. in their work. In addition, it was proposed that there was no regenerator in the model. This small value of thermal efficiency (about 14%) while the Carnot efficiency reaches nearly 62.5%. They got a convergence solution up to velocity 1860 rpm after that it diverges due to the transfer of the flow to turbulent. Their results emphasize the poor assumption of constant heat transfer coefficient in the second-order analysis because of non-uniform temperature within Stirling engine. Moreover, they concluded that impingement heat transfer has an absolutely huge impact on cooling and heating working gas inside Stirling engine.

From the literature, it can be summarized that the 2^{nd}-order analysis predicts the performance of Stirling engine less accurately compares the CFD model due to large error value in heat transfer coefficient. Another reason for that is coming from the assumption of uniform temperature distribution which is not correct as found from CFD models. Furthermore, it is found from the experimental work that the power output vary according to the Stirling engine size and the operational boundary conditions. Additionally, the Stirling engine reflects small thermal efficiency when there is no regenerator.

However there is great effort are done on Stirling engine, but still, there are some gaps which required to be filled. For instance, all of the CFD models ignore radiative heat

transfer without indicating that whether it has an impact on the performance of the engine or not. Also, a lot of work focused on the regenerator part in order to improve the thermal efficiency while they the thermal efficiency can be improved also by the design of the heater and the cooler shapes.

Table 2.1 Setup summary of CFD literature review

	Author	Validation	Engine type	Motion mechanism	Gas type
1	Dyson et al. [42] (2005)	1D code & experimental data.	Free piston	-	He
2	Mahkamov[10] (2006)	Experimental	Gamma	Crank shaft	N_2
3	Mahkamov and Ingham [40],[41] (2006)	None	Alpha	Crankshaft	He
4	Lin et al. [43] (2011)	Experimental data	Free piston	-	He
5	Ibrahim [28] (2012)	Experimental data	-	Crankshaft	Air
6	Costa et al.[29] (2013)	Experimental correlations.	-	-	Air
7	Costa et al. [44] (2014)	Empirical correl.	-	-	-
8	Salazar and Chen [45] (2014)	Thermodynamically	Beta	Rhombic	Air
9	Zhigang Li et al. [30] (2014)	Analytical reciprocating flow in pipe	Alpha	Ross	He
10	Chen et al.[33] (2014)	Thermodynamically (adiabatic compression)	Gamma	Crank-shaft	air
11	Alfarawia et al.[34] (2014)	-	Beta	Crank-shaft	-
12	Costa et al.[35] (2014)	-Experimental	-	-	-
13	Costa et al.[36] (2015)	Correlation work in literature.	-	-	-
14	Chen et al. [39] (2015)	Other's work	Beta	Rhombic	Air

Table 2.2 Main results of summary of CFD literature review

	Comments (main results)
1	• η_{Carnot}=62%, η_{model}=32%, $\eta_{exp.}$=32% • The model over-predict indicated power compared to 1D model (Sage code).
2	• Two factors limiting power output; regenerator loss and dead volume. • 2^{nd}-order predicts the indicated power output with ~30% accuracy while this value decreases to 12-18% for CFD model.
3	• Standard k-ε model for compressible flow. • 2^{nd}-order analysis predicts double the power obtained using CFD analysis.
4	• η_{Carnot}=62%, η_{model}=33%, $\eta_{experiment}$=28.5%
5	• A high pressure drop occurs in the regenerator (87%) at 90 and 270 C.A due to high velocity. • Error in heat transfer coefficient fluctuates between 23% and 75%.
6	• Drive a correlation for pressure drop friction factor for a wound wire woven function in (d) and Re<400
7	• Get correlations for stack and wound woven wire matrices which covered range: 4<Re<400, wire dia. 0.08-0.11 mm, volumetric porosity 0.6-0.68 • Nu for the wound is lower by 20% than stack woven matrices. • No influence of porosity.
8	• The regenerator is not included in the study. • η_{Carnot}=62.5%, η_{model}=14%, • Major heat transfer occurs due to impingement of the gas. • Heat transfer coefficient is not constant as treated in 2^{nd}-order.
9	• Porous sheet regenerator has high power output due to low entropy generation • η_{model}=44%, η_{carnot}=67%
10	• η_{carnot}=25%, ηmodel=5%. • There was difference in their result and those obtained by second-order analysis especially in heat transfer coefficient. • highly non-uniform temperature distribution
11	• η_{carnot}=47%, η_{model}=40% • Geometry simulation carried out by SolidWorks • Uniform temperature distribution achieves by change heater angle of deflection
12	• Come up with a correlation between friction coefficient factor and Re • They simulate only the regenerator (3D)
13	• Staked configuration has better overall performance compared to a wound woven wire matrices
14	• Porosity increase pressure losses, however, the output power and thermal efficiency were improved.

CHAPTER 3

MATHEMATICAL FORMULATION

3.1 Problem Formulation

In this CFD simulation, a β-type Stirling engine driven by a rhombic mechanism is adopted. It is same geometry in Salazar and Chen work [45]. It consists of three zones; compression zone, expansion zone, and narrow zone which connects the expansion and compression zones as shown in Figure 3.1. In general, this narrow channel is filled with regenerator materials, however in this work, it is the regenerator is excluded for simplification. Also, from the same figure it easy to notice that the problem could be solved as axis-symmetric geometry. So that, only half of the domain is simulated. The dimension of the simulated geometry is reported in Table 3.1.

Table 3.1. Dimensions of the β-type Stirling engine in (mm).

r_1	20
r_2	20.5
G	5
$l_{1=}\ l_{2=}\ l_{3=}\ l_4$	18
L_t	158
L	42
L_{pt}	50.93
L_{dt}	163.74
l_d	79.46
R_d	3.5
δ	1

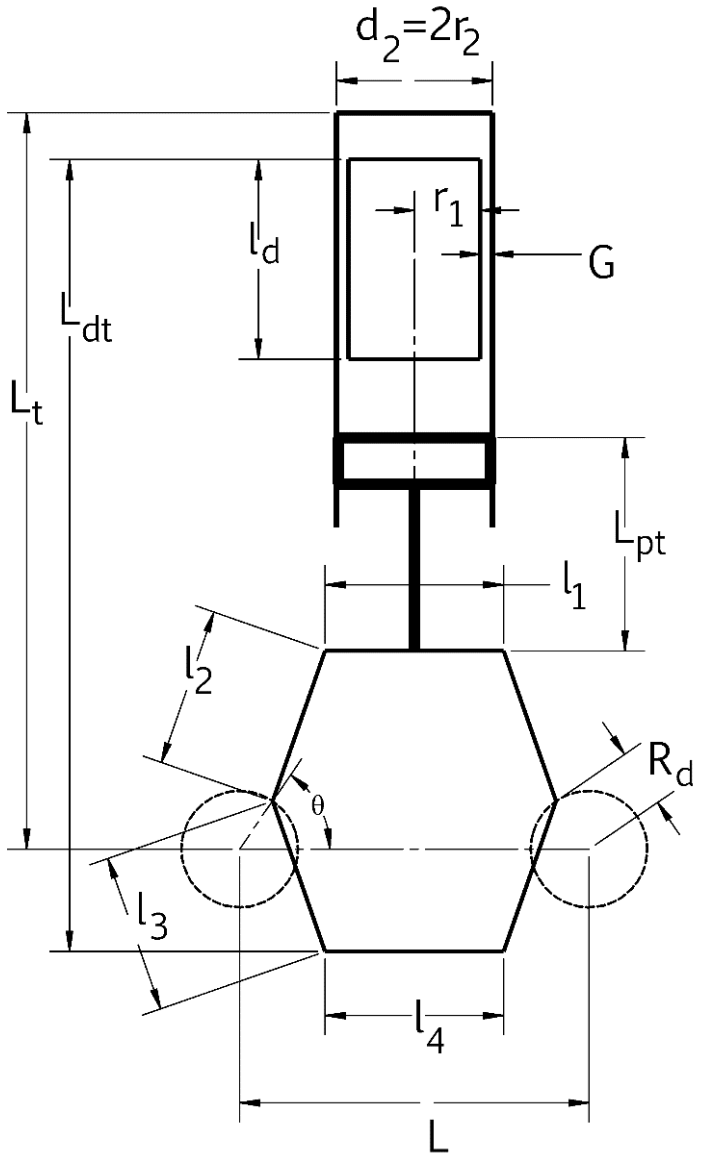

Figure 3.1 β-type Stirling Engine

The transport equations describing the flow fields and heat transfer phenomena inside Stirling engine are embodied mathematically by transient axisymmetric compressible Never-Stokes equation, conservation of energy equation, conservation of mass and ideal gas equation. Those equations are described as:

The continuity:

$$\frac{\partial \rho_f}{\partial t}+\frac{\partial}{\partial x}\left(\rho_f \tilde{u}\right)+\frac{1}{r}\frac{\partial}{\partial r}\left(\rho_f r\tilde{v}\right)=0 \tag{3.1}$$

The momentum:

$$\begin{aligned}
&\frac{\partial}{\partial t}\left(\rho_f u\right)+\frac{\partial}{\partial x}\left(\rho_f \tilde{u}u\right)+\frac{1}{r}\frac{\partial}{\partial r}\left(\rho_f r\tilde{v}u\right)=\rho_f g-\frac{\partial p}{\partial x}+\mu\frac{\partial}{\partial x}\left(\frac{\partial u}{\partial x}\right)+\frac{u}{r}\frac{\partial}{\partial r}\left(r\frac{\partial u}{\partial r}\right)+\frac{\mu}{3}\frac{\partial}{\partial x}\left(\nabla.V\right)\\
&\frac{\partial}{\partial t}\left(\rho_f v\right)+\frac{\partial}{\partial x}\left(\rho_f \tilde{u}v\right)+\frac{1}{r}\frac{\partial}{\partial r}\left(\rho_f r\tilde{v}v\right)=-\frac{\partial p}{\partial r}+\mu\frac{\partial}{\partial x}\left(\frac{\partial v}{\partial x}\right)+\frac{u}{r}\frac{\partial}{\partial r}\left(r\frac{\partial v}{\partial r}\right)+\frac{\mu}{3}\frac{\partial}{\partial r}\left(\nabla.V\right)-\frac{\mu v}{r^2}
\end{aligned} \tag{3.2}$$

The energy:

$$\begin{aligned}
\frac{\partial}{\partial t}\left(\rho_f T_f\right)+\frac{\partial}{\partial x}\left(\rho_f \tilde{u}T_f\right)+\frac{1}{r}\frac{\partial}{\partial r}\left(\rho_f r\tilde{v}T_f\right)=&-\frac{1}{c_{pf}}\left[\frac{\partial p}{\partial t}+\nabla.\left(pV\right)-p\left(\nabla.V\right)\right]+\frac{k_f}{c_{pf}}\left[\frac{\partial}{\partial x}\left(\frac{\partial T_f}{\partial x}\right)+\frac{1}{r}\frac{\partial}{\partial r}\left(r\frac{\partial T_f}{\partial r}\right)\right]\\
&+\frac{\mu}{c_{pf}}\left\{2\left[\left(\frac{\partial u}{\partial x}\right)^2+\left(\frac{\partial v}{\partial r}\right)^2+\left(\frac{v}{r}\right)^2\right]+\left(\frac{\partial v}{\partial x}+\frac{\partial u}{\partial r}\right)^2-\frac{2}{3}\left(\nabla.V\right)^2\right\}
\end{aligned} \tag{3.3}$$

Ideal gas equation:

$$pV=\rho_f RT_f \tag{3.4}$$

Where $\tilde{u}=u-u_c$, $\tilde{v}=v-v_c$ are relatively velocity components between the fluid and moving frames with velocities of u_c and v_c in x and r direction, respectively.

As starting point a parametric study for proposed geometry and motion mechanism (Figure 3.1) is conducted. It included three types of working fluid and different operational temperature limits and initially charge pressure boundary conditions. Then the study extended to take account of radiative heat transfer. Hence, different radiation models are examined and the influence of radiation heat transfer on the Stirling engine performance is

demonstrated. After that, the performance of the proposed Stirling engine is trying to be enhanced by attaching different heater and cooler shapes. Moreover, different motion mechanisms and various Stirling engine configuration are investigated. More details are shown in following subtitles.

3.2 Parametric Study of β-type Stirling Engine

As a starting point, a parametric study includes three types of working fluid; air, helium, and hydrogen were performed. These gasses are the most common used as working fluid for Stirling engine. Also, N_2 gas is used to operate Stirling engine [46] [47], however, it does not include in this study because it has almost similar thermal properties as air gas. Each one of these fluids was tested for a range of charged pressure between 1 bar to 5 bar to obtain the optimum value for the generated power and the efficiency except for hydrogen it extended up to 12.5 bar to get the optimum point. The effect of initially charged pressure is conducted at minimum wall temperature (T_C) of 300 K and maximum wall temperature (T_H) of 800 K. The external wall exposes to a variable temperature which is a function of x-coordinates:

$$T(x)=\begin{cases} T_C\ (\mathrm{K}), & \text{if } x \le 0.08 \text{ m} \\ T_C+\dfrac{x-0.08}{0.158-0.08}\left(T_H-T_C\right)\ (\mathrm{K}), & \text{if } x > 0.08 \text{ m} \end{cases} \tag{3.5}$$

Additionally, the effect of T_H in Equation 3.1 is examined for a range of 800 K to 1300 K while T_C and the initially charged pressure were kept at 300 K and 1 bar, respectively. Also, the range of maximum and minimum temperature was shifted to a higher lever by a step of 100 K until T_C reach up to 800 K and T_H reach value of 1300 K. This is to see which operation range is the best for this type of Stirling engine. For all the

cases under study, the Stirling engine is set to rotate at a speed of 1800 rpm. Also, the thermal properties of the three working fluid were taken as variable with the temperature. The cylinder wall has a thickness of 1 mm and it is made of steel. It has properties of density (7840 kg/m^3), thermal conductivity (43 m^{-1}.K^{-1}) and specific heat (450 J.kg^{-1}.K^{-1}).

Initially, the gas is at 300 K and cylinder wall temperature is given by Equation 3.1 which is not a function of time. The cylinder head and the piston were kept at T_H and T_C all the time, respectively. Additionally, displace is set to be insulated so no heat transfer will go through it. Moreover, the movement of the piston and displacer are governed by a rhombic motion as shown in Figure 3.1. The velocity of this kind of motion is represented by:

$$u_p(t) = R_d\omega\left\{\cos\theta - \sin\theta\left[l_2{}^2 - \left(\frac{L}{2} - \frac{l_1}{2} - R_d\cos\theta\right)^2\right]^{-0.5}\left[\frac{L}{2} - \frac{l_1}{2} - R_d\cos\theta\right]\right\}$$
$$u_d(t) = R_d\omega\left\{\cos\theta + \sin\theta\left[l_2{}^2 - \left(\frac{L}{2} - \frac{l_4}{2} - R_d\cos\theta\right)^2\right]^{-0.5}\left[\frac{L}{2} - \frac{l_4}{2} - R_d\cos\theta\right]\right\} \quad (3.6)$$

The left gear in Figure 3.1 rotates in a clockwise direction, as a result, a negative value of rotation speed (ω) was used in above equations. The motion starts from a crank angle of zero degree.

On the other hand, the cylinder walls of Stirling engine are exposed to a conduction heat transfer in the radial direction and it is energy equation for this case is given by Fourier's law:

$$q = -k\frac{\partial T}{\partial n} \tag{3.7}$$

Since the partial Equations 3.1, 3.2 and 3.3 have been solved numerically, the supplied and rejected heat transfer were calculated as following:

$$\begin{aligned} Q_{in} &= \frac{\omega}{2\pi}\sum_{i=1}^{N} Q_i.\Delta t \quad if \quad q > 0 \\ Q_{out} &= \frac{\omega}{2\pi}\sum_{i=1}^{N} Q_i.\Delta t \quad if \quad q < 0 \end{aligned} \tag{3.8}$$

Where Δt is time step. Q_{in}, $Q_{out,}$ and Q_i are the total heat added, total heat rejected and total heat transfer during the step (i). Q_i is calculated across the boundaries S_H, $S_{R,}$ and S_C as shown in Figure 3.1. While the power output calculated numerically from:

$$W_{out} = \frac{\omega}{2\pi}\sum_{i=1}^{N} 0.5(p_{i-1} + p_i).(\mathrm{V}_i - \mathrm{V}_{i-1}) \tag{3.9}$$

Where p is average pressure at specified zone, and V is the volume that zone.

3.3 Radiative Heat Transfer Implementation

Radiation heat transfer is the third part of heat transfer modes. Since the energy transfer by means of electromagnetic waves in radiation heat transfer, it does not require a medium like convection and conduction heat transfer. The importance of radiation heat transfer appears in many engineering applications, particularly at high temperatures. It contributes noticeably to energy transfer in combustion chambers, furnace, high-temperature heat exchanges, and during the explosion of chemicals. Although, it can be important even at low temperature levels and plays a major role in explaining different

phenomena. For instance, ice could be formed from water in plastic cover at night time. Considering convection heat transfer only would fail to explain this phenomenon without radiative heat transfer, where heat loss occurs by emitting energy to the cold heat sink of the night sky. Because of all that, the radiative heat transfer is involved in this study to show its influence on the performance of Stirling engine. So that, the three modes of heat transfer; conduction, convection and radiation would be included.

Two types of radiation modeling were examined in this work. The first one is a surface-to-surface (S2S) model, which account for the radiation exchange in an enclosure of gray-diffuse surfaces. In S2S model any absorption, emission or scattering of radiation by the medium can be passed over.

Therefore, the heat flux leaving a given surface (k) is composed of emitted and reflected energy as follows:

$$q_{out,k} = \varepsilon_k \sigma T_k^4 + \rho_k \sum_{j=1}^{N} F_{kj} q_{out,j} \tag{3.10}$$

Where $q_{out,k}$ is the energy flux leaving surface (k), $q_{out,j}$ is the heat flux from the surroundings, ε_k is the emissivity, σ is the Stefan-Boltzmann constant and F_{kj} is the view factor which is the fraction of energy leaving surface (k) that is incident on surface (j).

It is calculated as:

$$F_{kj} = \frac{1}{A_k} \int_{A_k} \int_{A_j} \frac{\cos\theta_k \cos\theta_j}{\pi r^2} \delta_{kj} dA_k dA_j \tag{3.11}$$

Where δ_{kj} =1 if dA_j is visible to dA_k and zero otherwise.

The other model of radiation that used in this study is Discrete Ordinates (DO) Radiation Model. However the DO model solve the radiative heat transfer equation by taking into account the effect of absorption, emission and scattering, but here in this work the coefficients of absorption, emission and scattering are set to zero as working fluid is not radiation participating medium.

The general form of the radiative transfer equation (RTE) for an absorbing, emitting, and scattering medium is:

$$\frac{dI\left(\vec{r},\vec{s}\right)}{ds}+\left(a+\sigma_s\right)I\left(\vec{r},\vec{s}\right)=an^2\frac{\sigma T^4}{\pi}+\frac{\sigma_s}{4\pi}\int_0^{4\pi}I\left(\vec{r},\vec{s}'\right)\Phi\left(\vec{s}\cdot\vec{s}'\right)d\Omega' \tag{3.12}$$

For the gray diffuse radiation, the net radiative heat flux leaving the surface is given by:

$$q_{out}=(1-\varepsilon_w)q_{in}+n^2\varepsilon_w\sigma T_w^4 \tag{3.13}$$

Where q_{in} is the incident radiative heat flux:

$$q_{in}=\int_{\vec{s}\cdot\vec{n}>0} I_{in}\vec{s}\cdot\vec{n}\,d\Omega \tag{3.14}$$

The DO model is more computationally expensive than S2S model because it transform RTE into a transport equation for radiation intensity, then it is solved as many transport equation as there are direction $\vec{s}$. In this work, the working fluid (medium) inside Stirling engine does not participate in radiative energy, so that the scattering, emitting, and absorbing coefficients would be zero. Accordingly, only radiation between surfaces would be solved.

3.4 Heater and Cooler Shapes Optimization

The heater and cooler in the proposed geometry (Figure 3.1) is a simple cylinder exposes to high temperature at the top head while the lower side of the cylinder is kept at low temperature. In this part of the study, the heating and cooling surfaces are enlarged by attaching different fins shape. In particularly, three fins profile have been tested. The first profile has a single triangular fin joined to the cylinder top where high temperature is supplied, and another one at bottom of the cylinder where Stirling engine exposes to low temperature as shown in Figure 3.2**.** The second shape is similar to the first one but with five triangular fins instead of only one fin. Each fin has a width of 0.5 mm and height of 10 mm with 0.5 mm distance between the fins. In the third fin profile, the five triangular fins have replaced by other five annular cylinder shape as explained in Figure 3.2. A small gap of 0.01 mm is added to the cylinder side in order to avoid software errors coming from the deforming walls due to the motion of the piston. In all cases, the engine is running by air with atmospheric initial charged pressure. It has a speed of 1800 rpm and it utilizing rhombic mechanism. Thus same velocity profile in Equation 3.6 is used in this part of the study. The top of the cylinder and the adjacent fins surfaces are kept at 800 K. The cylinder wall just beneath top fins up to a distance of 78 mm far from the top has a linear temperature profile from 800 K to 300 K while the remaining cylinder wall and fins below that distance are kept at 300 K.

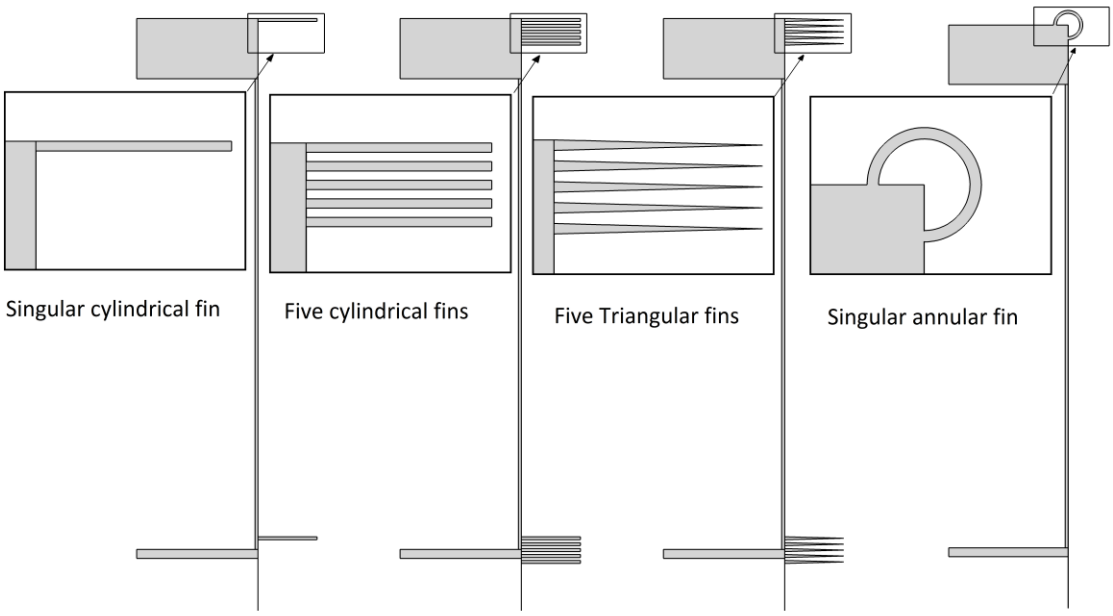

Figure 3.2 Different Heater/Cooler fins profile shapes.

3.5 Piston Motion Mechanisms Investigation

The motion mechanism of the piston plays a significant role in the heat transfer in Stirling engine since it controls the movement of working fluid inside the chambers. It controls how fast the gas moves from the hot chamber to the cold chamber in order to be compressed and vice versa. The importance of the motion mechanism becomes clear during compression and expansion process. For instance, in the compression process, it is preferred to have all of the working fluid in the cold zone, so the energy required to compress the gas would be small. Nevertheless, it is difficult to achieve that. There is always an amount of gas in the other zone (hot zone). As a result, some of the gas will expand during the compression process which increases the required compression power. Therefore in this portion of the work two other mechanisms have performed beside of

rhombic mechanism. These mechanisms are simple crankshaft and scotch mechanisms as drawn in Figure 3.3.

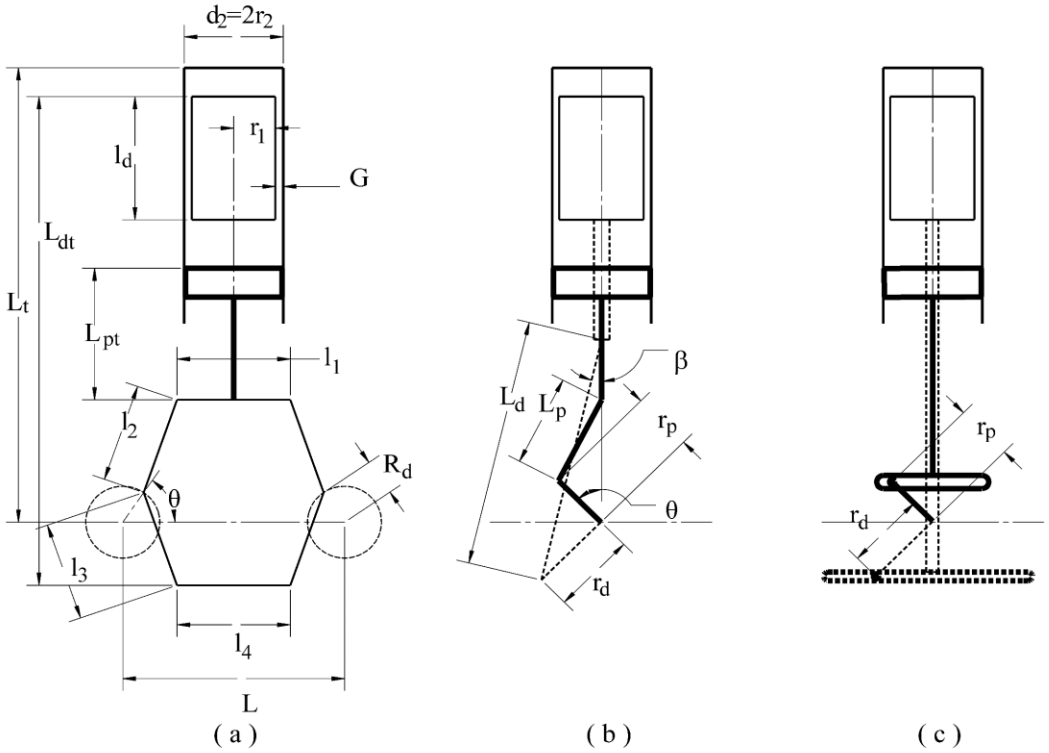

Figure 3.3 Stirling engine motion mechanisms; (a) Rhombic, (b) Crankshaft, and (c) Scotch mechanism.

Similar operational boundary conditions of temperature and pressure are applied in this part of the study. A temperature boundary conditions of Equation 3.5 are utilized. Additionally, an air with atmospheric initially charged pressure is used as working fluid. All of three mechanisms have the same rotational speed of 1800 rpm. Moreover, all case are set to start from same initial volume, so they will have the same amount of air mass inside the engine. This initial volume is corresponding to the volume in the geometry of Figure 3.1 with (θ=0°). Furthermore, they are set to have an approximately similar value of the maximum and minimum total volume. The velocity illustrated in Equation 3.6 is

used for rhombic. While the velocity of the crankshaft and scotch mechanisms can be described by Equations 3.15-3.19. The corresponding geometry dimensions of these equations are described in Table 3.2.

Crank-shaft mechanism velocity:

$$u_p = r_p \omega \cos\theta - \frac{r_p^2 \omega \cos\theta \sin\theta}{\sqrt{L_p^2 - r_p^2 \cos^2\theta}} \tag{3.15}$$

$$u_d = r_d \omega \cos\beta - \frac{r_d^2 \omega \cos\beta \sin\beta}{\sqrt{L_d^2 - r_d^2 \cos^2\beta}} \tag{3.16}$$

$$\beta = \theta + \pi/2 \tag{3.17}$$

Scotch mechanism velocity:

$$u_p = -r_p \omega \sin\theta \tag{3.18}$$

$$u_d = -r_d \omega \sin\beta \tag{3.19}$$

Table 3.2 Dimension parameters used in crank-shaft and scotch mechanisms.

Parameters	Crank-shaft mechanism	Scotch mechanism
r_p	5.05	5.05
r_d	4.975	4.975
L_p	14.033	-
L_d	5.127	-

Since in the crankshaft and scotch mechanisms the motion does not start from θ=0 (to have the same initial volume as in rhombic mechanism where $\theta_{rhombic}$ start from zero), it is required to add shifted angle to θ in order to have the right velocity at the beginning (t=0).

The shifted angle for the proposed geometry driven by crankshaft and scotch mechanisms are 0.81623487 and 0.94252011 rad, respectively.

3.6 Stirling engine Configurations Study

There are three Stirling engine configurations; Alpha, Beta, and Gamma. The schematic and dimensions of the three types are presented in Figure 3.4 and Table 3.3. Two geometry of α-type Stirling engine is proposed. In the first geometry, the connecting pipe has a cylindrical shape, while it has an annular shape in the second geometry as described in Figure 3.4 (a and b). In this part of the study, a performance comparison of these types is performed. Since the previous studies and the model validation are done for β-type Stirling engine, so that, β-type is considered as the base case. Hence, other configurations (Alpha and Gamma types) are managed to have same swept and initial volumes as in β-type. The base case has same dimensions described in Table 3.1**.** All Stirling engine types are set to work with air as working fluid. Also, a crank shaft mechanism is adopted for this part of the study. However, the crankshaft radius and connection rode length vary between the configurations. The reason for that is to have same swept volume and initial volume as in the base case (β-type). The three engines types run at 1800 rpm with atmospheric charge pressure.

In Figure 1.5, it has been shown that γ-type consists of two separated cylinders connected with a pipe. The large cylinder containing the displacer and the small cylinder having a power piston. The geometry by this mean it required to be simulated as 3D geometry. However, a small modification can be done in order to solve the problem as 2D

axis-symmetry. This modification is done by eliminating the connection pipe and then putting the small cylinder just below the large cylinder as shown in Figure 3.4d.

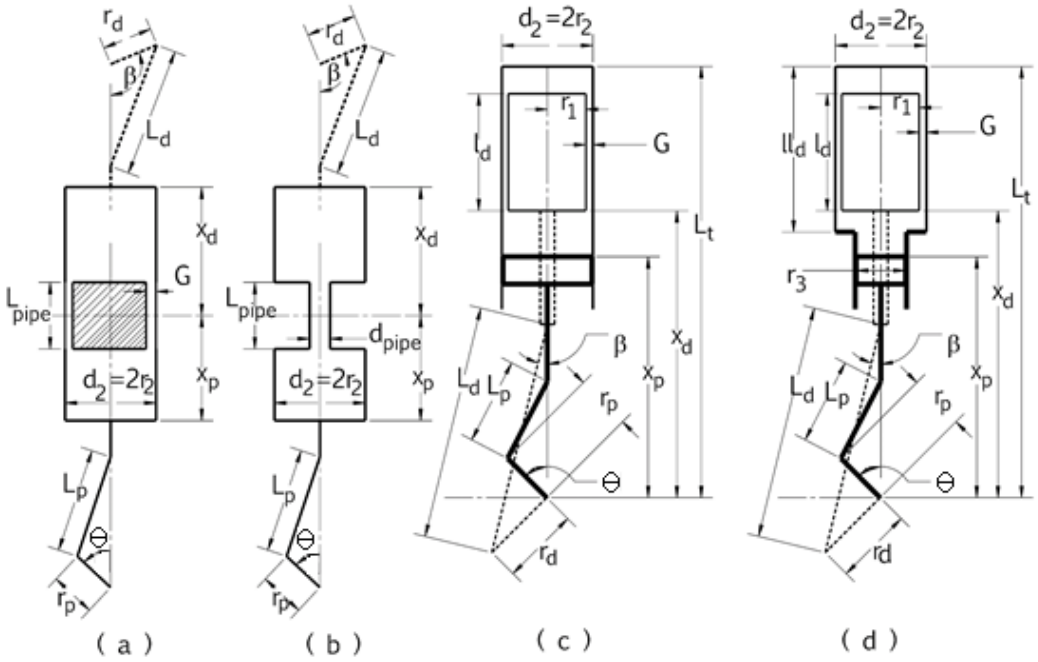

Figure 3.4 Stirling engine configurations; (a) Alpha, (b) Beta, and (c) Gamma types.

Table 3.3 Geometry dimensions for α, β, and γ-types of Stirling engine (mm).

	α-type	β-type	γ-type
d_{pipe}	4.5	-	-
G	-	0.5	0.5
l_d	-	79.46	80.5
ll_d	-	-	90
L_d	30	51.273	45
L_p	30	14.033	30
L_{pipe}	80	-	-
L_t	-	158	158
r_1	-	20	20
r_2	20.5	20.5	20.5
r_3	-	-	15
r_d	3.536	4.975	4.375
r_p	3.536	5.05	9.339

The new geometry of γ-type becomes similar to β-type but with small cylinder size in the bottom. The diameter of the cylinder that containing displacer is equal for γ- and β-types. Nevertheless, the displacer length and the stroke length are different so that minimum volume, maximum volume, and swept volume would be equal for the two types of Stirling engine. In the third Stirling configuration (α-type), the cold chamber and hot chamber diameters are set to 20.5 mm which is same cylinder diameter in the β-type Stirling engine. Again, the crankshaft radius and connecting rod length are managed to produce same minimum volume, maximum volume, and swept volume as in a β-type Stirling engine. Moreover, in order to simulate the problem as 2D axis-symmetry, the two cylinders are arranged in one line.

In β- and γ-types Stirling engine, the boundary conditions of Equation 3.5 are adopted. While in α-type Stirling engine, the cylinder head and side are set at 800 K and 300 K for hot and cold zone respectively. Furthermore, the piston in the cold zone is set at a constant temperature of 300 K as it can be cold by external water flow. In contrast, the piston at hot zone is considered as insulated boundary conditions since it can't be heated because it may cause motion problems. Moreover, the temperature of the connecting pipe wall is varied linearly from 300 K at top cylinder head of the cold zone to 800 K at top cylinder head of the hot zone. For α-type Stirling engine the temperature boundary condition is governed by:

$$T(x)=\begin{cases} T_C(K), & if \quad x \le -0.04\,m \\ T_C+\dfrac{0.04-x}{0.08}\left(T_H-T_C\right)(K), & if \quad -0.04<x<0.04\,m \\ T_H(K), & if \quad x \ge 0.04\,m \end{cases} \tag{3.20}$$

3.7 Numerical Procedure

In order to solve the governing Equations 3.1-3.3, a general purpose code of ANSYS fluent 15 was used. The program uses a finite volume method to discretize these differential equations. The second order up wind was adopted for continuity, momentum and energy equations. Furthermore, the flow type is assumed to be laminar flow because maximum Re (based on the hydraulic diameter of the narrow channel) does not exceed the laminar range for all of the cases under study. However in some cases, *Re* becomes in the transitional range (2,000-4,000) but the flow does not convert to fully turbulent flow. One of the software limitation is that it cannot solve laminar and turbulent flow at the same time, so it should only solve for either laminar flow or turbulent flow. Since the dominated region of the flow has *Re* less than 2,000 so that laminar flow model is utilized. Although with *Re* greater than 4,000 the laminar flow can occur by using wall material with small roughness. In this work the flow is confined to laminar flow, however, the study can be extended to turbulent flow.

The temperature profile described in Equations 3.5 and 3.20 and the piston and displacer motion mechanisms (Equations 3.6 and 3.15-3.19) are implemented in the software through a user-defined function (UDF). The conduction heat transfer through the external walls which described in Equation 3.7 has not been included in the computational domain. Nevertheless, the wall properties and its thickness were defined in the wall

boundary condition so the software will solve the conduction heat transfer without needs to be drawn in computational geometry. The errors convergence were set to 1e-6 for all governing equations; continuity equation, momentum equations and energy equation.

In addition, a COUPLE scheme was utilized with the intention of couple the pressure and velocity values instead of SIMPLE scheme, because it shows a relatively fast convergence compare to SIMPLE scheme. The SIMPLE scheme uses a pressure-based segregated algorithm in which the momentum equation and the pressure correction equation are solved separately. This semi-implicit solution method results in slow convergence [48].

CHAPTER 4

RESULTS AND DISCUSSION

4.1 Dynamic-mesh Validation

Before starting the numerical simulation of Stirling engine, the dynamic mesh is validated by simulating an adiabatic compression of air in a single cylinder with a piston govern by sinusoidal motion. Since there is no friction or heat loss were taking into account, the reversible adiabatic cycle is described by:

$$PV^k = C \quad , where\ k = \frac{c_p}{c_v} \tag{4.1}$$

In the numerical simulation, adiabatic compression process can be achieved by running the piston at very low speed (1 rpm). Additionally, all cylinder walls should be set as zero heat flux (i.e. it is insulated). So that an equilibrium state will be valid. Figure 4.1 shows a comparison of the CFD work and the adiabatic cycle results in term of static pressure. It is clear that they are totally identical.

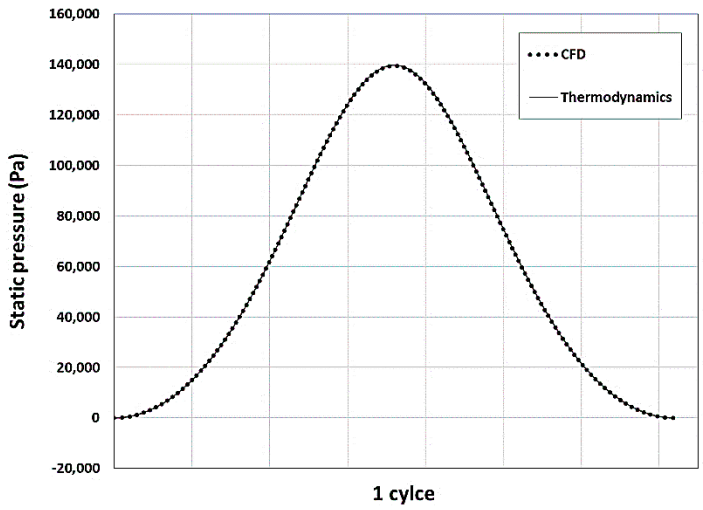

Figure 4.1 A comparison of adiabatic compression process done by CFD and analytical thermodynamic model.

Then the simulation is extended to include Stirling engine. A mesh and time dependence study were carried out for the geometry described in Figure 3.1 and Table 3.1. Four different mesh sizes were tested. They have a cells numbers of 2740, 6869, 9600 and 15020 cells. Furthermore, more dense mesh is included in the narrow space. It consists of 10, 14, 16 and 20 intervals, respectively. In fact, the dense mesh in the narrow channel will lead to higher aspect ratio in the expansion and compression zones. Therefore in the coarse mesh, a small number of an interval within narrow channel was selected. While in the fine mesh, a large number of interval was used in the narrow channel. By this way, the aspect ratio for all mesh under study was kept between 10.5 and 11.8. Moreover, each one of these mesh sizes was tested with three step-number per cycle of 360, 480 and 720 step/cycle with are corresponding to a time-step interval of 9.25926×10^{-05}, 6.94444×10^{-05} and 4.62963×10^{-05} seconds. It was found that mesh size of 6869 cells with 480 step/cycle (i.e. .94444

x10^{-05} s) achieve the mesh and time-step independence solution with an error of 0.6% in generated power compared to the finest mesh size with the smallest time step.

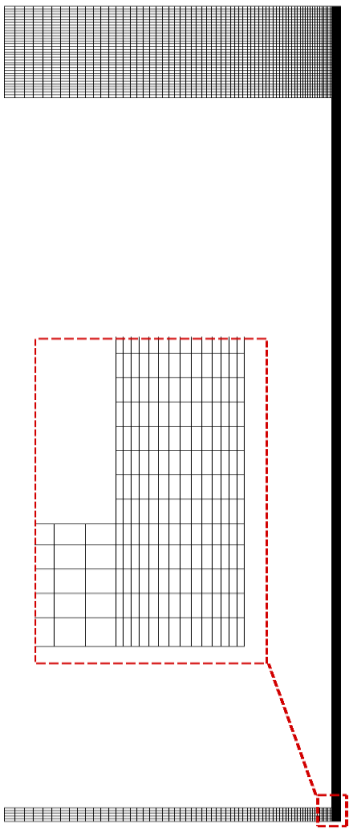

Figure 4.2 Computational meshed domain of beta-type Stirling engine.

In addition, it worth to mention that for simulated Stirling engine the domain is scaled up by 10^{12} then it returns back to the original size in Fluent software by scaling down by 10^{-12} in order to compensate 32-bit precision available in grid generation especially when there is fraction length as recommended by [42].

After that the model was compared with the work of Salazar and Chen [45] for the same boundary conditions. The only difference is that, in Salazar and Chen work, they utilized

constant thermal properties for the working fluid. However, here in this work, variable thermal properties were utilized to make the problem much close to the real case. Hence, an ideal gas equation which represented in Equation 3.4 was used to calculate gas density while the kinetic theory was used to identify the heat capacity and the viscosity. Figure 4.3 shows a comparison of P-V diagram for the expansion and compression chambers. It is clear that there are well matching between the two results. However, there is slightly less power output with a magnitude of (7.7 W) was obtained in the present work compare to the value of (11.7 W) in Salazar and Chen's result. This difference is mainly due to the usage of variable thermal properties which is the more realistic than taking the thermal properties at an average value of T_H and T_C.

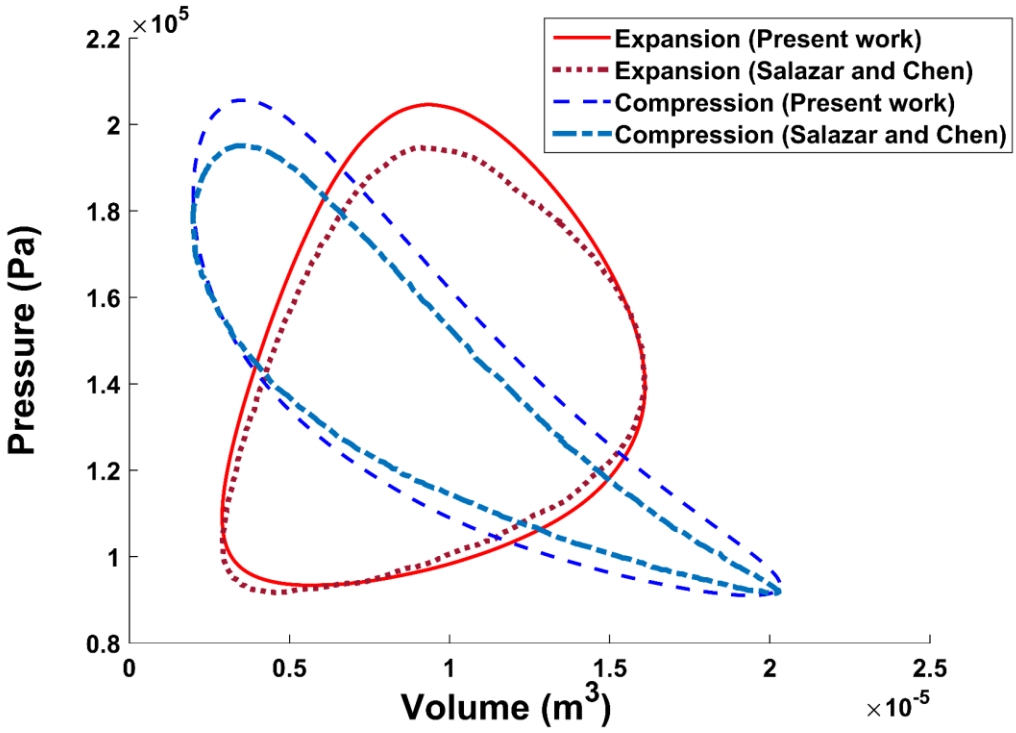

Figure 4.3 P-V diagrams of expansion and compression zones comparing between the present work and Salazar and Chen's work [45].

Then, the effect of viscous heating dissipation (the last term in Equation 3.3) was tested and it turns out there is a little bit difference in temperature results, thus, it can be negligible. Also, the gravity effect was tested as well, and it turns out it has no impact on the engine performance. So no viscous heating nor gravity effects were included in the present study.

4.2 Parametric Study of β-type Stirling Engine

A comprehensive operational parametric study was carried out. These parameters include; initially charge pressure, operational temperature limits and the type of the working fluid. In order to illuminate the influence of these parameters on Stirling engine performance, 60 cases were examined in this study.

4.2.1 Effect of Initial Charge Pressure

The impact of initially charge pressure on heat transfer, work output, and thermal efficiency is shown in Figure 4.4. In cases where the air is used as working fluid; the Stirling engine produces only 7.8 W at atmospherically charge pressure with an efficiency of 7.8%. As the initially charge pressure increases, the engine becomes more tend to absorb a higher amount of heat. Accordingly, the power generated from the Stirling engine increased slightly to the maximum of 8.15 W at charged pressure of 1.75 bar.

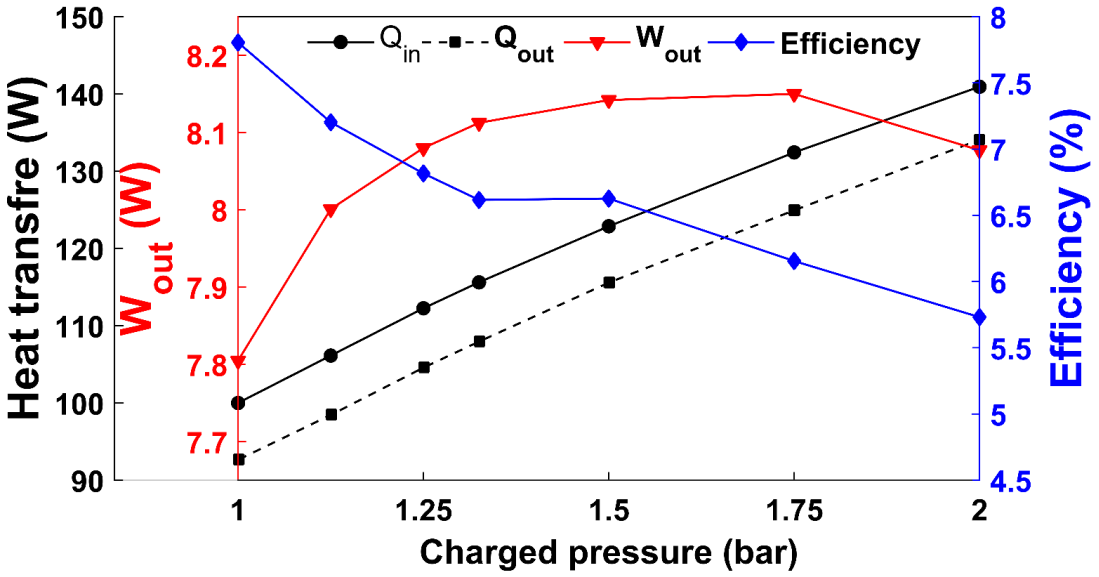

Figure 4.4 β-type Stirling engine performance at different charge pressure and temperature limits of 300-800 K for air gas.

At large charge pressure value, the flow starts to convert into turbulent flow. Up to charge pressure of 2 bar, the *Re* number (based on the hydraulic diameter of the narrow channel) remains within a laminar region which is our concern in this work. After that, the flow goes to turbulent in a small portion of the cycle. In particular, high *Re* number occur at the narrow channel when the displacer moves downwards and the piston moves upward (i.e. when they move toward each other). Moreover, the efficiency curve starts from 7.8% at atmospheric pressure then it falls gradually until it reaches the smallest value of 5.7% at 2 bar.

On the other hand, when the working fluid was changed from air to helium gas both of efficiency and power output were improved dramatically as shown in Figure 4.5. With helium gas at atmospherically charge pressure, Stirling engine produces 14 W with an

efficiency around 14.9%. These values are almost double that obtained from the air as working fluid with the same charge pressure.

Helium gas has a kinematic viscosity much greater than air. Thus, small *Re* number could be obtained even at large charge pressure. This allows extending the parametric study up charge pressure of 4 bar within the limits of laminar flow. After 4 bar charge pressure, the flow starts to convert into a turbulent regime which is not considered in this study. Among these charge pressure limits, the maximum power extracted from Stirling engine is 19.6 W. It occurs at 2.5 bar which is greater than the charge pressure that achieves optimum power output in the case of air gas.

In addition, the efficiency curve obtained from He gas has a similar pattern as that of the air but on a larger scale. It has supreme value at low charge pressure (1 bar) then it falls down gradually as charge pressure increases. Therefore, it starts from 14.9% at atmospheric pressure then it drops gradually to 9.1% at 4 bar.

However, the extreme power output achieved at 2.5 bar, but it is preferred to operate the Stirling engine at 2 bar. The reason for that can easily be noticed from the efficiency and power output curves in Figure 4.5. The power output will not be affected very much by reducing the charge pressure to 2 bar. On the other hand, the efficiency will increase from 12.1% to 13.3%.

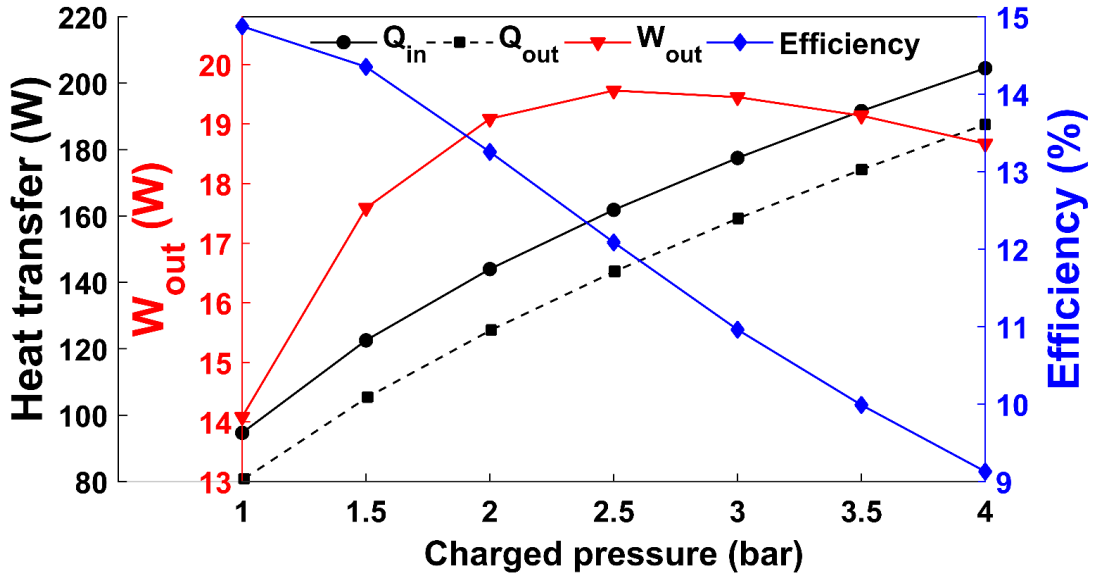

Figure 4.5 β-type Stirling engine performance at different charge pressure and temperature limits of 300-800 K for He gas.

Further improvement in power output was obtained by utilizing Hydrogen gas (H_2) as working fluid. The hydrogen gas is known to have the highest thermal conductivity of all gasses. As a result, a tremendous amount of heat could be absorbed as shown in Figure 4.6. As the mass inside the Stirling engine increases (by increasing charge pressure) the engine becomes more able to absorb a large amount of heat due to high thermal conductivity of hydrogen. This gives Stirling engine a chance to generate large power output by using H_2 gas instead of using air or He gasses. Even at atmospheric pressure H_2 gas generates power much greater than maximum power produced by air at optimum charge pressure (17.3 W for H_2 at 1 bar and 8.15 W for air at 1.75 bar). The greatest power generated by H_2 gas is 65.2 W (with an efficiency of 7.4%) which is obtained at 12.5 bar. While at the peak thermal efficiency (11.2%) the output power is relatively low (39.3 W)

which is recorded at 2.5 bar. Moreover, from Figure 4.6 it can be easily noticed that charge pressure from 7.5 bar to 12.5 bar has almost same values of power output. However, the corresponding efficiency diminishes as charge pressure increases.

So, similar to the operation with helium gas it would be a wise decision to operate the Stirling engine charged with H_2 gas at a pressure below the optimum one of the power output (12.5 bar) and above the optimum pressure of thermal efficiency (2.5 bar). For instance, if the engine runs at 7.5 bar instead of 12.5 bar the efficiency would improve from 7.4% to 9.3%. Thus, only 685.5 W would be required as Q_{in} instead of 881.6 W. But in return, there would be a reduction in output power by only 1.5 W.

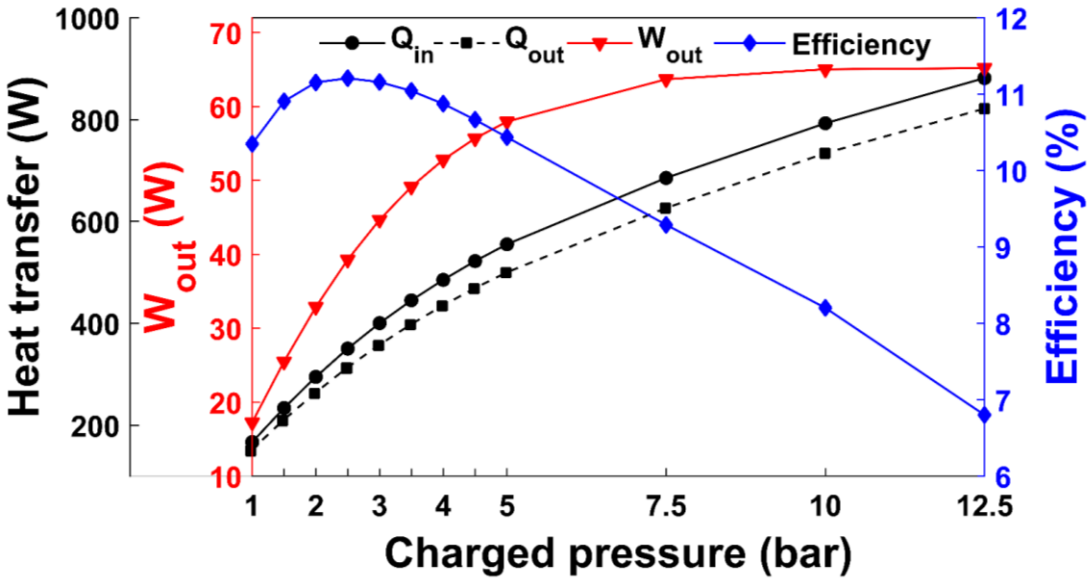

Figure 4.6 β-type Stirling engine performance at different charge pressure and temperature limits of 300-800 K for H2 gas.

Additionally, a curve fitting was conducted for efficiency and power output in Figure 4.4 to Figure 4.6. Since the efficiency profile of hydrogen gas has a bell shape, a Gaussian function was proposed to fit the efficiency curve as following:

$$\eta_{th}(x) = a_1 e^{\frac{-(x-b_1)^2}{2c_1}} + a_2 e^{\frac{-(x-b_2)^2}{2c_2}} \tag{4.2}$$

Where $a, b \; and \; c$ are constants shown in Table 4.1 and x is the charge pressure. While the power output was represented by polynomial functions as:

$$W_{out}(x) = d_1 x^4 + d_2 x^3 + d_3 x^2 + d_4 x^1 + d_5 \tag{4.3}$$

Where d is constant shown in Table 4.2 for the three working fluid.

Table 4.1 Coefficients of efficiency fit curve equation 3.22

	Air	He	H_2
a_1	1.272	6.559	3.539
b_1	-1.331	-1.839	-0.8899
c_1	0.5267	1.773	1.054
a_2	6.69	9.836	9.044
b_2	-0.6116	0.05627	0.5221
c_2	5.651	4.184	3.107

Table 4.2 Coefficient of generated power fit curve equation 3.23**.**

	Air	He	H_2
d_1	-2.484	-0.2419	-0.7
d_2	15.65	0.7482	5.011
d_3	-37.06	-1.176	-13.54
d_4	39.17	0.206	16.77
d_5	-7.463	19.55	56.88

For the three gasses (Air, He and H_2) the performance of the beta-type Stirling engine is examined for charge pressure starting from atmospheric pressure, then the charge pressure increases gradually until the flow becomes laminar at 2 bar, 4 bar and 12.5 bar for air, He and H_2, respectively. Therefore Equation 4.2 and 4.3 are valid for laminar flow range.

Moreover, it has been found that at any moment of time the temperature distribution is highly non-uniform within the chambers as displayed in Figure 4.7. In order to characterize the heat transfer behavior, the temperature contours were observed at various time during one complete cycle. Figure 4.8 shows temperature contours at different cycle time for hydrogen gas at 4 bar charge pressure. Focusing on the expansion chamber it can be noticed that as displacer comes close to the top dead center (TDC) its velocity approaches zero and the fluid velocity also becomes very small. Thus, low amount of convective heat transfer occurs. By referring to Figure 4.9 which represents heat transfer on top and bottom of the cylinder; this period of no fluid motion demonstrates the declination in heat transfer on the cylinder head (i.e. the declination after step number 270 of the dashed line). Therefore, only fluid layers near the heating walls would have high temperature compared to another area in expansion chamber due to diffusion heat transfer mainly. Then heat transfer rate rises up quickly due to movement of the displacer toward bottom dead center (BDC) pushing the gas from compression chamber to the expansion zone. The cold jet gas coming through narrow channel would hit the cylinder head resulting in impingement heat transfer which is known as the most effective convective heat transfer mechanism (see Figure 4.8). As the displacer moves away from TDC the vortex that made by impingement of fluid on cylinder head also travels with it. Hence, the effect of

impingement heat transfer degrades slowly as the vortex moved away from the cylinder head. On the other hand, monitoring heat transfer on the bottom of the cylinders shows a zig-zag fluctuation. It mainly happens due to the velocity of the piston. So that due to non-uniform temperature distribution across the engine the assumption of constant convective heat transfer coefficient in some second-order model could not reflect the real state of Stirling engine. This leads to an error on its performance. Similar results were noticed in other CFD simulations of Stirling engine [33][45].

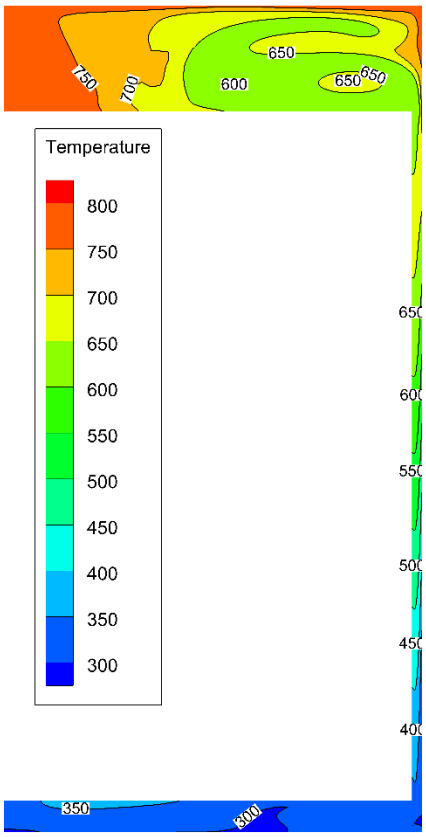

Figure 4.7 Temperature contours inside β-type Stirling engine using H_2 gas at 4 bar charge pressure and temperature limits of 300-800 K.

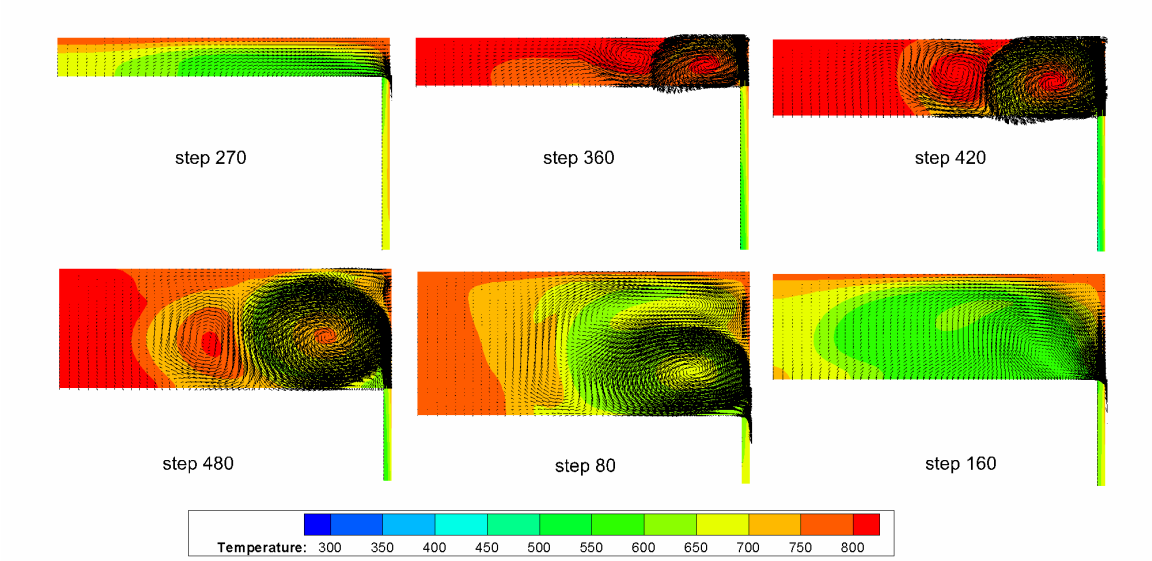

Figure 4.8 Temperature contours and velocity vectors at expansion chamber at various steps for H_2 gas at 4 bar and temperature limits of 300-800 K.

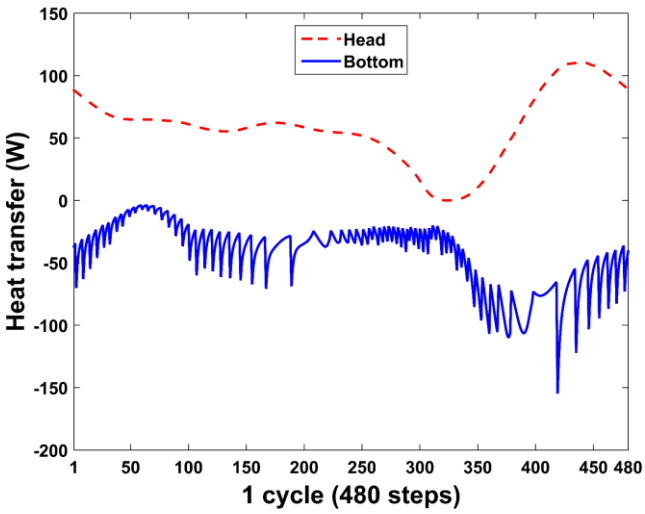

Figure 4.9 Heat transfer at top and bottom of the cylinder for the case of H_2 gas at 1 bar charge pressure and temperature limits of 300-800 K.

Besides non-uniform temperature distribution, there is small pressure variation within the Stirling engine at any given time during the cycle. Nevertheless, this variation is a tiny fraction of total pressure, but it leads to an error in power output calculated from Equation 3.9 and power output obtained from the differences between heat added and

rejected from the system (Equation 3.8). Even in Salazar and Chen [45], it seems to be there was an error of 18% between the net heat transfer and generated power. They got values of 82.5 W, 69.7 W and 11.7 W for heat input, heat output and generated power respectively. The source of this error is coming from the pressure variation across the whole engine volume. So that taking the average pressure of the entire volume would lead definitely to mistake in power output value. In order to reduce this error, the complete volume should be divided into many zones. Then the output power for each zone could be calculated separately through the p-v diagram. Then the total power output is the summation of the power from these zones. In this work, the total volume was divided into three zones (expansion zone, regeneration zone, and compression zone) and the average pressure was monitored for each zone separately. By this way, the error between net heat transfer and output power would diminish because the pressure variation within these small zones is less than pressure variation within the total volume. However, as the initial charge pressure increases the error value grows because that would make more pressure difference even in the divided small zones. In contrast, as the difference between the operational temperatures (T_H-T_C) becomes large the pressure distribution becomes more uniform. Thus, a small error in power calculation would be obtained. Figure 4.10 shows the error between net heat transfer and total power output calculated from the p-v diagram of an expansion and compression zones.

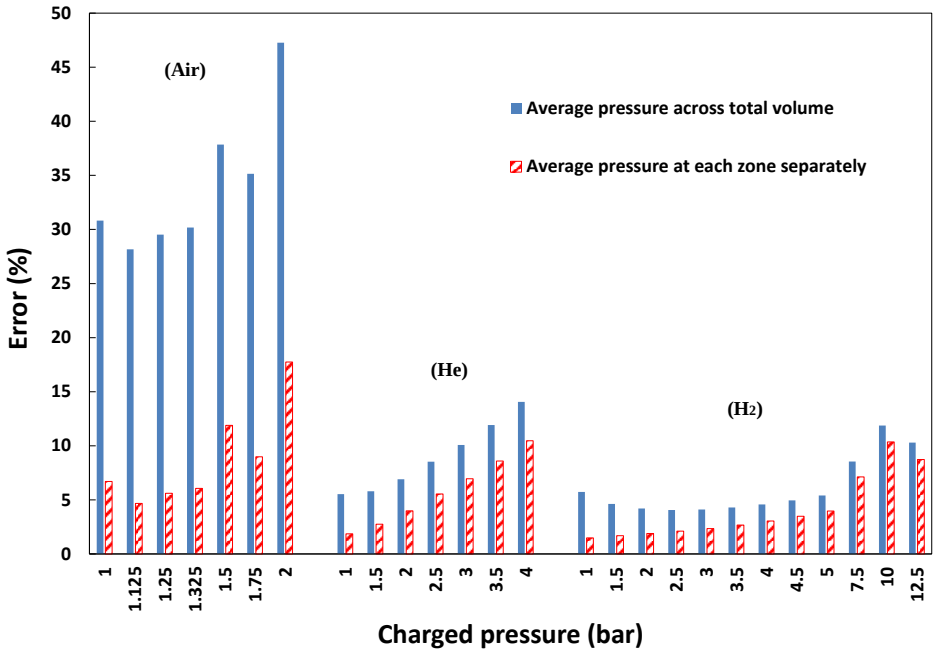

Figure 4.10 Error in the power output due to taking average pressure at each chamber separately.

4.2.2 Effect of Heater Temperature (TH)

In this part of the parametric study, the gas charge pressure was taken to be atmospheric. Also, the temperature of the cold side T_C remains at 300 K while heater temperature T_H increased gradually from 700 K up to 1300 K by an increment of 100 K. The limit of 1300 K is high, however, there is some material can endure this temperature without reaching the melting temperature range such as steel and cast-iron [49]. Figure 4.11a depicts the indicated power versus T_H for various working fluid (Air, He and H_2). It can be seen that the power increases almost linearly with increases in T_H. Additionally, in all T_H ranges under study; air registers the lowest indicated power, while hydrogen recorded the largest amount of power output. Also, Figure 4.11a shows that the slope of the power output for the He gas is higher than the slope of air and H_2 gasses. This indicates that at low T_H the He gas produces less power output than H_2 gas. However, as

the T_H rises up, the generated power from He gas increases faster than the power generated from H_2 gas. Thus, at high T_H (for instance, at 1300 K) He and H_2 gases produce almost same amount of power output (31.9 W and 32.9 W for He and H_2 gases, respectively), while at that temperature air produces only 22 W. Furthermore, it is expected, when the T_H reaches 1500 K, using He gas would generate more power than that produced using H_2 gas. The corresponding efficiency for the three fluids is represented in Figure 4.11b. Again, air shows the lowest performance while He reflects the best efficiency curve.

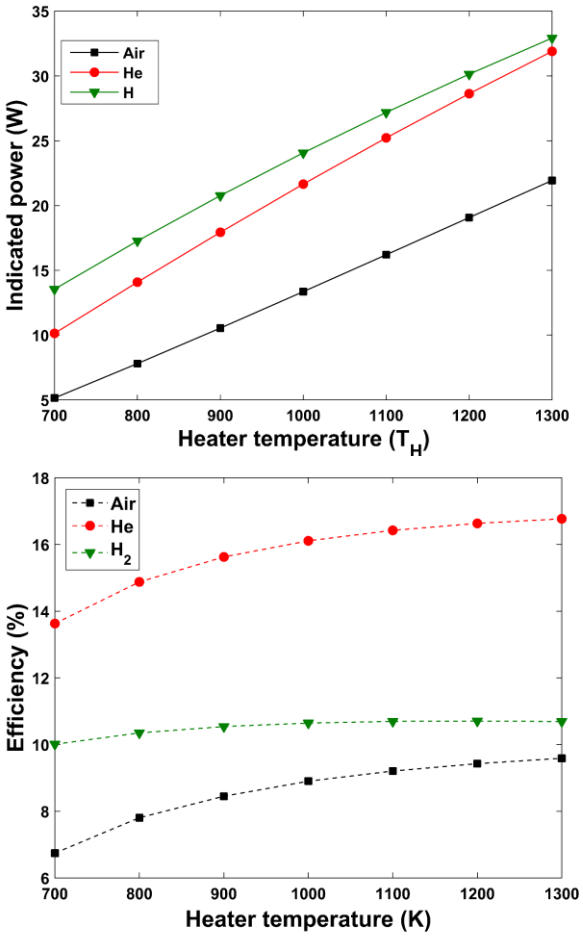

Figure 4.11 Effects of T_H on Stirling engine performance at 1 bar charged pressure and T_C of 300 K; (a) work output and (b) efficiency.

By comparing the efficiency curves of air and He, one can observe that increasing the differences between heater and cooler temperature has a positive impact on efficiency for both gasses. So that at heater temperature equivalent to 700 K (ΔT =400 K) both gasses gives the smallest values of efficiency (6.7% and 13.6% for air and He, respectively). Then it increases gradually as T_H increases, but with a small rate at a higher temperature. Moreover, the maximum efficiency values that were obtained are 9.6% and 16.8% at 1300 K for air and He, respectively.

On the other hand, hydrogen gas did not show any significant impact of heater temperature (T_H) on the improvement of efficiency, especially at high temperature. The efficiency starts from 10% at 700 K until it reaches about 10.7% and it remains at that level for T_H greater than 1000 K.

By remarking that at higher heater temperature both H_2 and He gasses generate almost same amount of power; besides at temperature greater than 1000 K the efficiency of H_2 gas remains around 10.7% while in He gas it exceeds 16%. Thus, at atmospheric charge pressure and high T_H, it is conclusively recommended to use He gas as the working fluid. Nevertheless, at low heater temperature (T_H < 1000 K) H_2 gas generates power greater by 10% than the power generated by He gas.

4.2.3 Effect of Shifting Temperature Limits (TH & TC)

In this part, the temperature difference ($T_H - T_C$) are kept constant at a value of 500 K. Figure 4.12a shows power output corresponding to operational temperature limits of (300-800 K) which have been shifted by step of 100 K until it reaches (800-11300 K) for T_C and T_H, respectively. The indicated power profiles are almost linear for all of the three

types of working fluid. It is similar to the previous section as operational temperature range shifted to a higher level, thus a large amount of heat would be transferred to Stirling engine. As a result, more power output could be extracted. In terms of efficiency, shifting the operational temperature range would result in a decline of the cycle thermal efficiency as shown in Figure 4.12b. When the engine work at high-temperature limits, it absorb large value of heat transfer, however, a large amount of heat is rejected also due to the high thermal conductivity of gasses at high temperature. Thus, a small increment of generated power occurs nevertheless this increment is very small compared to the absorbed heat energy at higher temperature limits. For instance, He gas at temperature limits of 300-800 K absorb 94.68 W to generate 13.83 W of useful power. In contrast, when it runs at temperature limits of 800-1300 K it absorbs about 257.8 W to generate only 26.71 W. In the second case the generated power is greater than the generated power in the first case, however, the second case has much higher heat supplied to the system which leads to small thermal efficiency.

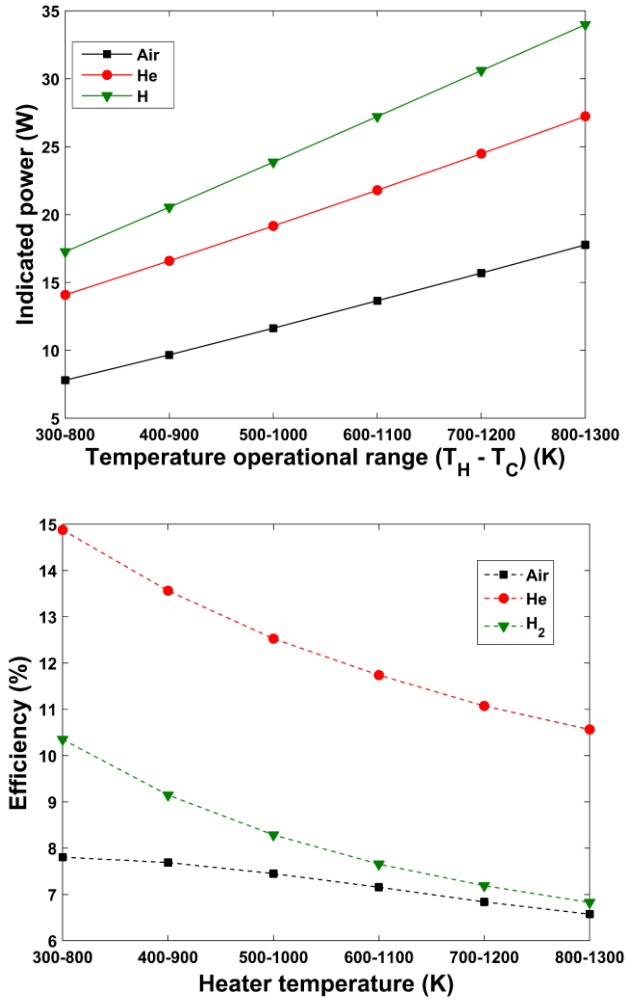

Figure 4.12 Effect of shifting operational temperature range on β-type Stirling engine performance at 1 bar charge pressure; (a) work output and (b) efficiency.

Table 4.3 Comparison of indicated power at different temperature limits.

T_H	T_{C1}/T_{C2}	Air		He		H_2	
800	300/300	7.8	7.8	14.1	14.1	17.3	17.3
900	300/400	10.5	9.7	17.9	16.6	20.8	20.5
1000	300/500	13.4	11.6	21.7	19.2	24.1	23.9
1100	300/600	16.2	13.7	25.2	21.8	27.2	27.2
1200	300/700	19.1	15.7	28.6	24.5	30.1	30.6
1300	300/800	21.9	17.8	31.9	27.2	32.9	34.0

Additionally, Table 4.3 represents a comparison of an indicated power at same T_H but with different T_C. All cases at 1 bar charge pressure. The first column represents cases of shifting T_H to high values while keeping T_C at 300 K which leads to rising up in ΔT. The second column represents a case of shifting operational temperature ranges to high values while keeping temperature difference constant. It has been noticed that using air and He produces larger power output as the differences between temperature limits (T_H and T_C) increases. For example at T_H equal to 1100 K; He gas produce 21.8 W (at T_C=600 K) while when temperature difference increased the engine produced 25.2 W (at T_C=300 K) for same source temperature. In contrast, hydrogen gas reflects different behavior. It shows a slight improvement in the power output as ΔT increases up to 700 K. As ΔT becomes greater than 700 K the generated power becomes less than that obtained from ΔT=500 K. For an operational range of (300-1300 K) and (800-1300 K), the first range produces 32.9 W while the later produces 34 W.

4.3 Impact of Radiative Heat transfer on β-type Stirling Engine

As explained previously, the impact of two radiation models (S2S and DO) are examined in this study. It conducted for a β-type Stirling engine with the rhombic mechanism that described in Table 3.1. The Stirling engine rotates with 1800 rpm and it utilizes air with variable thermal properties as working fluid.

Both radiation models (S2S and DO) have different parameter required to calculate the view factors for (S2S) model and to solve the discretized RTE. Accordingly, a sensitivity analysis for these parameters is required to ensure solution independence of these parameters. In S2S model, there are three parameters that control the accuracy of view

factor; resolution, subdivisions, and normalized separation distance (NSD). The NSD is the ratio of the minimum distance between the two faces to effective face diameter. If the NSD value is less than 5, the hemicube method calculates view factor more accurately than ray tracing method. In the proposed mesh there are some faces have NSD less than 5, therefore, hemicube method is adopted to calculate view factor with a NSD value of 5. The resolution and subdivisions parameters are tested for values of (10 and 5), (15 and 8), and (20 and 10). On the other hand in the DO model, the RTE solution should be independent of angular discretization parameters (number of divisions and pixels). For that reason, values of (2 and 1), (4 and 2), and (8 and 4) are tested for divisions and pixels values respectively.

Judging from the net heat transfer profile, it turns out that S2S radiation model parameters achieve accurate view factors by 15 and 8 as values for resolution and subdivisions, respectively. These values produce a maximum error of 0.26% in the net heat transfer profile. The error here is calculated under the assumption that the right solution is the solution which has the highest number of divisions and pixel values (case of 8 division and 4 pixels). While the angular discretization values for DO model becomes independent of divisions and pixel numbers by values of 4 and 2, respectively. The maximum error in the net heat transfer profile is 0.24%.

Figure 4.13 shows heat transfer profile obtained by S2S and DO models compared with the case of not taking radiative heat transfer into account. There is a good matching between the profiles of S2S and DO models through most of the cycle. However, in some part of the cycle, the S2S model underestimates rejected energy to the surrounding (step 150-300 in Figure 4.13). Also, it can be noticed from the same figure, ignoring radiative heat transfer

in the energy equation results in lower amount of gained and rejected heat transfer. Consequently, the output work would be less than output work obtained by considering radiative heat transfer.

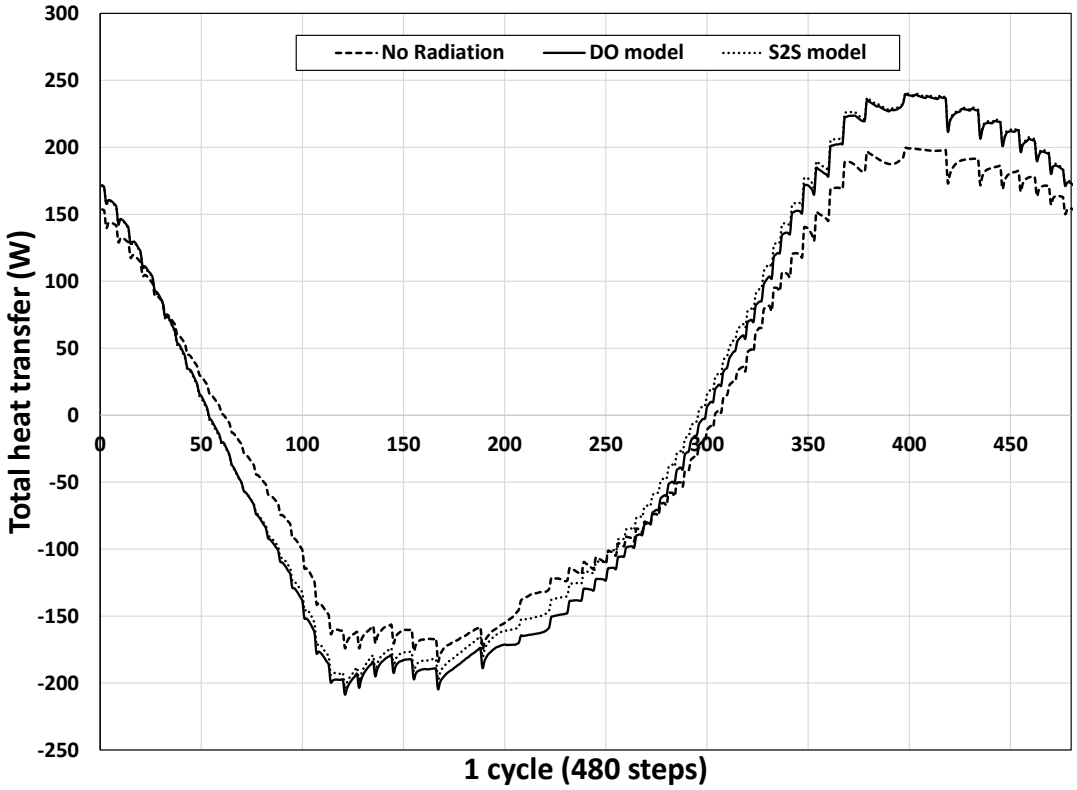

Figure 4.13 Radiation effect on heat transfer profile of β-type Stirling engine.

More comparisons in heat transfer, output work and efficiency are demonstrated in Table 4.4. In all cases, there are differences between the net heat transfer (Q_{net}) and the work calculated from PV-diagram (PV_{work}). For instance, the Do model reflects a net heat transfer value of 9.6 W, while the calculated PV_{work} is 9.9 W (3% error). This error is lower than the error in the case where on radiation is considered (4% error). In contrast, S2S model shows large error value between Q_{net} and PV_{work} (36%). Thus, DO radiative model is adopted in further proceeding analysis. Moreover, ignoring radiation energy yields to the error of 13% in gained and rejected heat transfer, while the useful output work and

efficiency are deflected from the right value by an error of 18%. These high value of errors clarify the importance of involving radiative heat transfer in the analysis of Stirling engine performance.

Table 4.4 Comparison of radiative model impact on Stirling engine performance.

	Q_{in} (W)	Q_{out} (W)	Q_{net} (W)	P*dV (W)	efficiency	Error in work
No Radiation	100.4	-92.6	7.9	8.2	7.8%	4%
DO model	116.0	-106.4	9.6	9.9	8.3%	3%
S2S model	118.6	-103.6	14.9	9.6	12.5%	-36%

4.4 Heater and Cooler Shapes Optimization

It is well known in heat transfer that a great enhancement in total heat transfer can be achieved by increasing the effective surface area. In Stirling engine, the heating and cooling area can be enlarged by adding internal fins as depict in Figure 3.2. The proposed fins increase the heating and cooling surface area by 53%, 226%, and 242% of the cases of the single cylindrical fin, five triangular fins, and five cylindrical fins. However, attaching these fins to the main body of Stirling engine leads to an increasing in the dead volume, which is not preferable. Therefore, this part of the study is aimed to reflect the impact of adding new surfaces (in the heating and cooling zones) on the performance of Stirling engine, and the consequence of the generated dead volumes due to fins installation.

Table 4.5 Performance of Stirling engine with different fin shapes.

	No Fins	Single cylindrical fin	5 triangular fins	5 cylindrical fins
Mass (kg/m3)	2.41E-05	2.61E-05	2.87E-05	3.37E-05
Heating/Cooling surfaces (m2)	1.44E-02	2.20E-02	4.69E-02	4.91E-02
Q_{in} (W)	116.0	105.9	115.8	126.2
Q_{out} (W)	-106.4	-96.9	-107.3	-119.1
Q_{net} (W)	9.61	9.0	8.57	7.12
Efficiency (%)	8.3%	8.5%	7.4%	5.6%

The highest power output is produced by the case where there are no fins installed (9.61 W) and the smallest one is produced by the case of five cylindrical fins (7.12 W). The reduction in the power output is primarily coming from the extra dead volume due to the fins. More explanation is demonstrated by Figure 4.14, which depict the average temperature in the expansion zone. It is clear that during compression process (step 180-400), all fins cases have higher temperature profiles compared to the no fins case. Higher temperature during the compression process results in higher pressure value (Figure 4.15). Consequently, a large amount of power would be consumed in the compression process, and hence, the power output decreases.

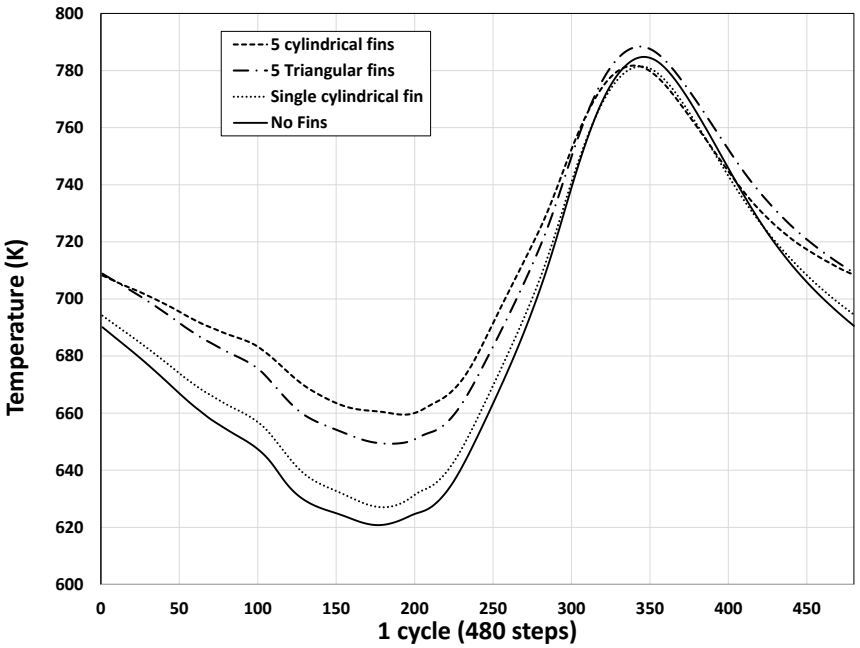

Figure 4.14 Average temperature profiles on the expansion chamber for different fins shapes.

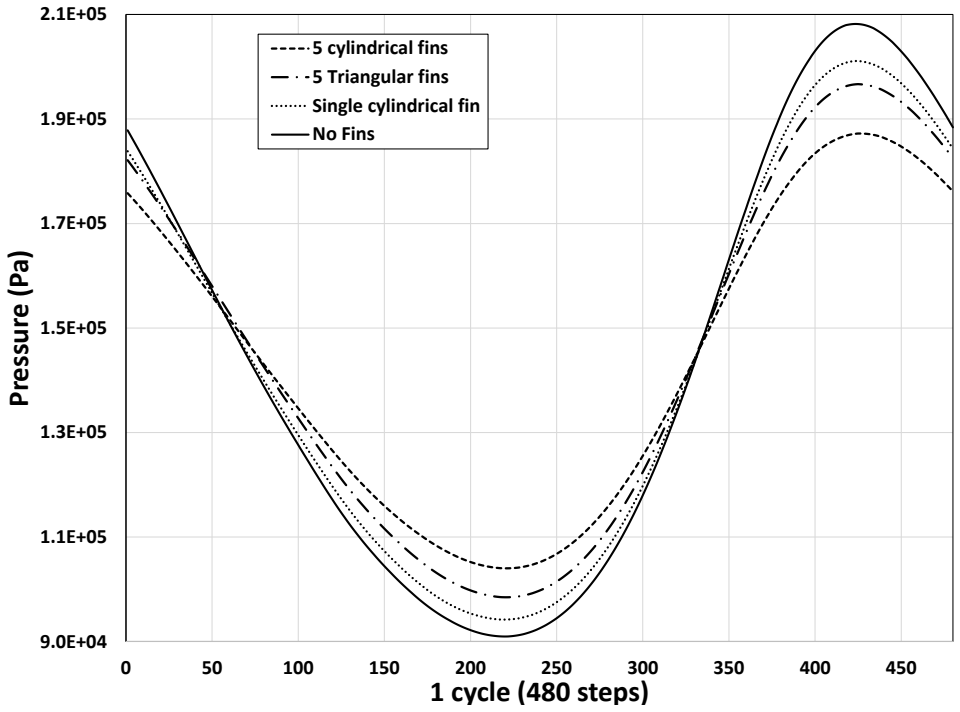

Figure 4.15 Average pressure profile for different fin shapes.

Moreover, the reduction of generated power due to fins implementation might be related to the fin orientations. It was noticed that the cylindrical and triangular fins (in Figure 3.2 a, b and c) do not allow gasses in the fin zone to circulate with other gasses in the compression and expansion zone. Hence, only the gas in the fin zone will be heated or cooled through the fins, while the remaining gas absorbs or rejects the heat energy through the cylinder head and the side walls. The unwell mixing of the gasses in the fin zone and other zones lead to make the fin dead volume has a negative impact on the Stirling engine performance. Therefore, a new fin shape is proposed (Figure 3.2d). It is an annular fin with circular cross section profile. One of the fin ends is connected to the cylinder head and the other end is connected to the cylinder side. Therefore, the gas is circulated and well mixed with other gas in the expansion zone. The annular fin is added only to the heating section. It results in 27% increasing in the surface area compare to the case of no fins installed.

Comparing with base case (without fins), the annular fin shape enhances the generated power output from 9.61 W to 9.96 W and the thermal efficiency increases from 8.3% to 9.3%.

4.5 Piston Motion Mechanisms investigation

One of the methods that play a significant role in Stirling engine performance is the type of motion mechanisms. It arranges the location of the working fluid to be in suitable place in the cold and hot chambers during the cycle. Figure 4.16 shows the heat transfer of rhombic, crankshaft, and scotch mechanisms during one cycle. The figure clarifies that the heat transfer values differ as the motion mechanisms are changed. Also, it is clear that the heat rejection process expands about the steps of 50 to 300. However when the heat rejection process start, not all of the working fluid is located in the cold chamber (compression zone).

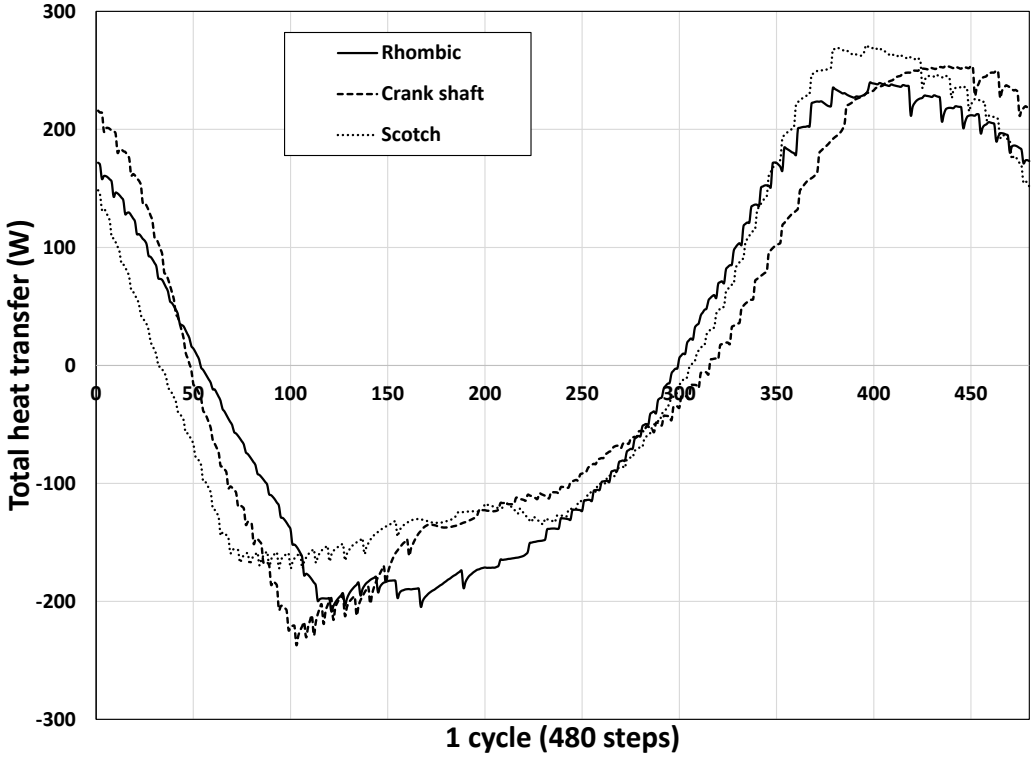

Figure 4.16 Heat transfer profiles for different piston motion mechanisms.

By taking rhombic mechanism as an example to demonstrate heat transfer, Figure 4.17 and Figure 4.18 show volume variation of rhombic mechanism and interesting points during the cycle when the piston and displacer reverse their direction. From Figure 4.18 at step number of 50, the displacer is moving up pushing hot gasses toward the cold chamber. At the same time, the piston moves downward making suction zone in the cold chamber, which helps hot gasses to flow into the cold chamber. As the hot gasses leave the hot chamber and enter the cold chamber, it collides with the piston resulting in high heat rejection due to impingement heat transfer. The heat rejection continues as long as the displacer moves upward pushing hot gasses to the cold chamber. When the displacer reach TDC (step 280) and reverse its motion direction, the cold gas flow toward the hot chamber. At that step (step 280), the piston is moving up helping cold gas to go to the hot chamber.

Once gasses are injected into the hot chamber, it starts to absorb heat (Figure 4.16). More gas is pushed into the hot chamber due to the upward piston motion. As a result, the amount of working gas inside the hot chamber increase which means more amount of heat absorption. Consequently, the pressure inside the engine increase dramatically as shown in Figure 4.19 (step 300-400). However, when the piston reaches TDC and reverses its motion direction, the pressure continue to rise up for few number of steps. Then the gas pushes the piston producing useful power. After that, the pressure falls down as engine volume expand. It is clear from Figure 4.19, in rhombic and scotch mechanisms the pressure reach high limit values (208184 and 205808 Pa, respectively). Thus, they generated a large amount of power output compared to crankshaft mechanism. A summary of engine performance for different piston motion mechanisms is shown in Table 4.6. Rhombic mechanism recorded the largest power output and thermal efficiency (9.6 W and 8.29%). Then it is followed scotch mechanism (9.4 W and 7.96%) While the crankshaft mechanism registers the lowest values of power output and thermal efficiency (8.5 W and 7.30%).

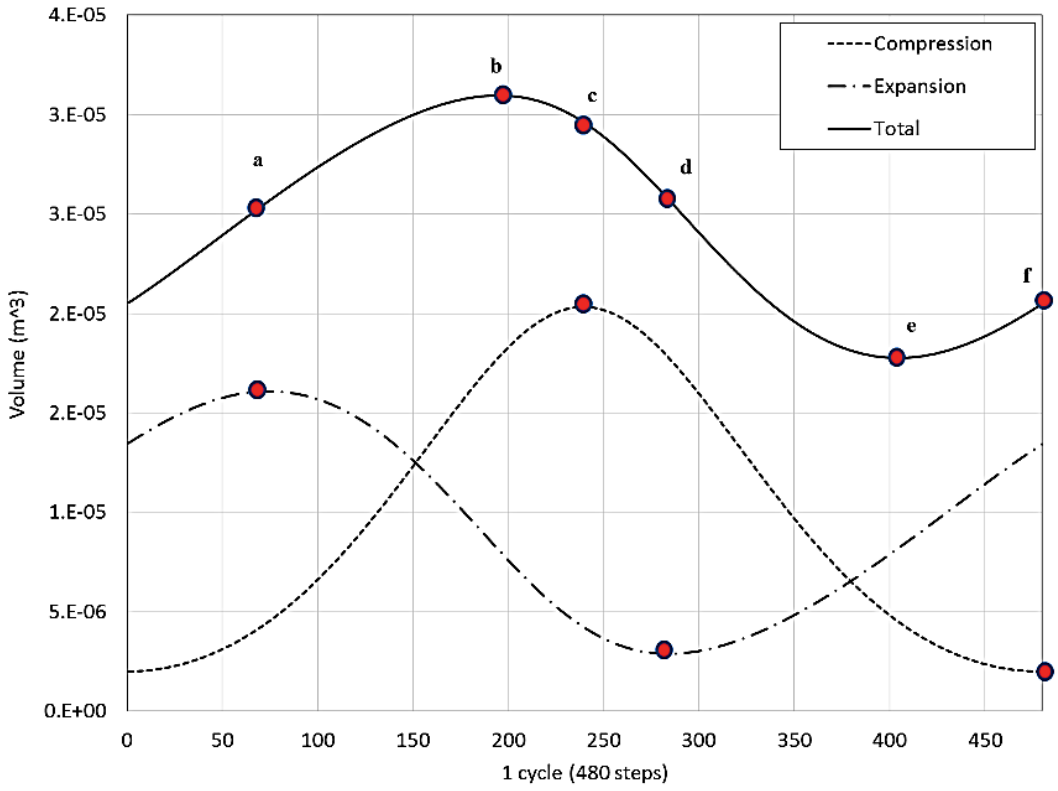

Figure 4.17 Volume change of rhombic mechanism.

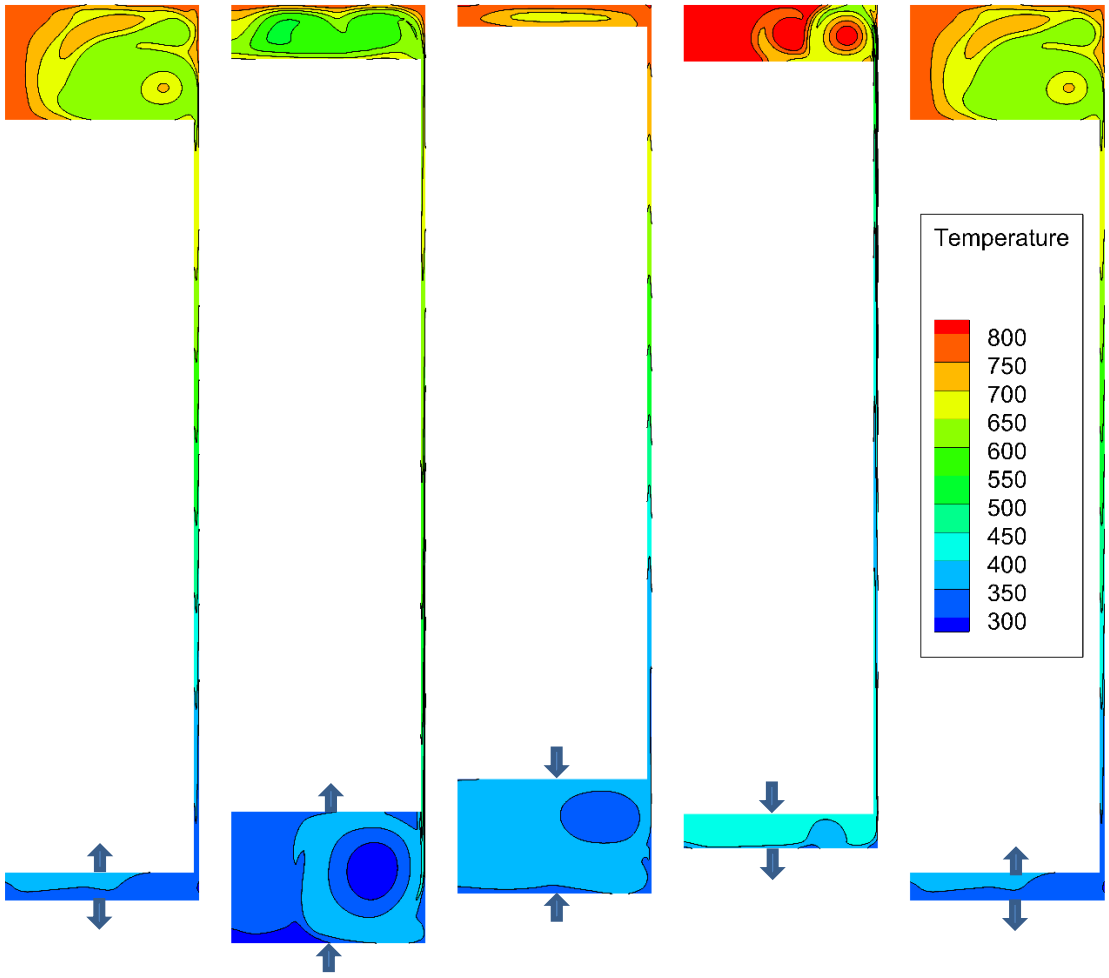

Figure 4.18 Positon and direction of the piston and displacer during one cycle for the rhombic mechanism.

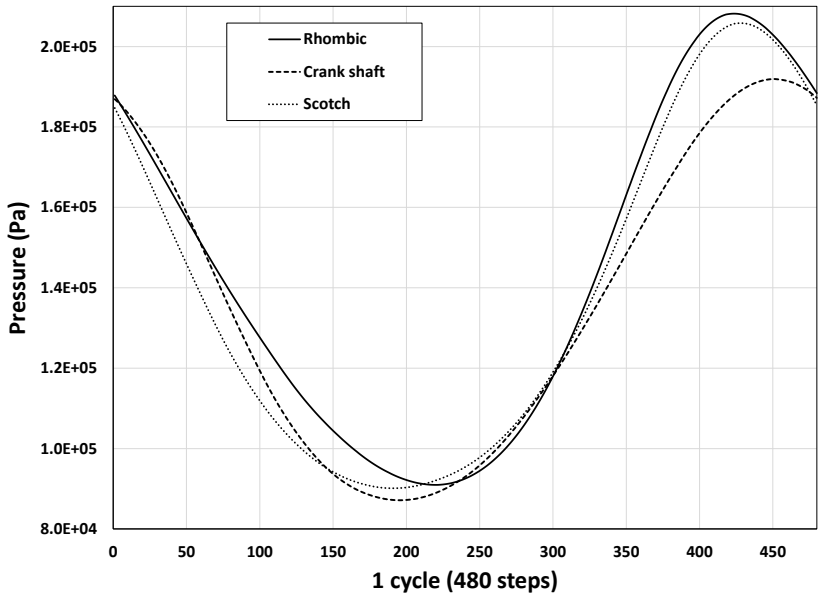

Figure 4.19 Pressure profile for different piston motion mechanisms.

Table 4.6 Engine performance under different piston motion mechanisms.

	Q_{in} (W)	Q_{out} (W)	Q_{net} (W)	W_{out} (W)	Efficiency
Rhombic	116.0	-106.4	9.6	9.90	8.29%
Crank shaft	116.8	-108.2	8.5	8.78	7.3%
Scotch	118.3	-108.9	9.4	9.69	7.96%

4.6 Stirling Engine Configuration Study

This part of study compares three configurations of Stirling engine (alpha, beta, and gamma). The three types of Stirling engine utilize air as working fluid and they are driven by crankshaft mechanism. Additionally, the initial volume and pressure are managed to be equal in all of the Stirling configurations. Table 4.7 summarize the performance of alpha, beta, and gamma types of Stirling engine. Beta-type Stirling engine recorded the lowest power output (8.5 W) among the three configurations with an efficiency of 7.3 %. The alpha-type with cylindrical pipe show a negative power output under the provided boundary condition. The reason for that may refer to large connecting pipe diameter, which allows working fluid to transfer from hot chamber to the cold chamber without making a significant reduction in its temperature, and vice versa when the gas moves from cold chamber to the hot chamber as shown in Figure 4.20. Therefore, the alpha-type Stirling engine is modified to have an annular connecting pipe instead of cylindrical connecting pipe. As a result, the new configuration generates a power output of 9.5 W, which is the largest power output value compare to the all other configurations. Also, the annular connecting pipe records the highest thermal efficiency (10.08 %). Gamma-type also has a high thermal efficiency (9.93 %), however, the generated power (9.4 W) is still less than power produced by the modified alpha types of Stirling engine (9.5 W). In all cases, it has been noticed that most of the heat transfer occurs in the narrow channel connecting the two

chambers (hot and cold) as shown in Figure 4.21. In the case of alpha-type with the cylindrical connecting pipe, it can be easily seen that the heat transfer occurs in the connecting pipe is very small compared to other Stirling engine types (beta, gamma, and alpha type with annular connecting pipe). Thus, the total heat transfer is very small which lead to a negative power output.

Table 4.7 Engine performance for different Stirling engine configurations.

	Qin (W)	Qout (W)	Qnet (W)	Wout (W)	Efficiency
Alpha (cylindrical pipe)	25.4	-26.9	-1.4	-0.68	-
Alpha (Annual pipe)	94.2	-84.7	9.5	9.88	10.08%
Beta	116.8	-108.	8.5	8.78	7.30%
Gamma	94.8	-85.4	9.4	9.27	9.93%

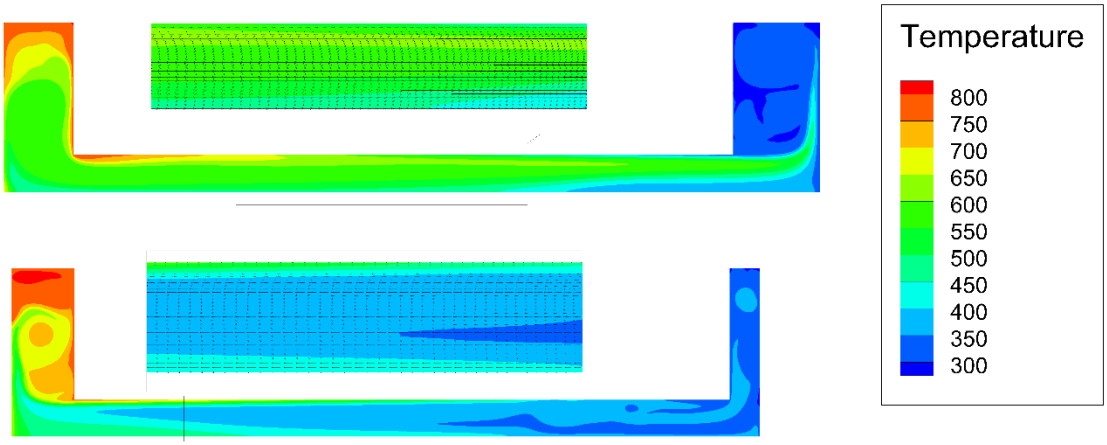

Figure 4.20 Temperature contours for the alpha-type Stirling engine.

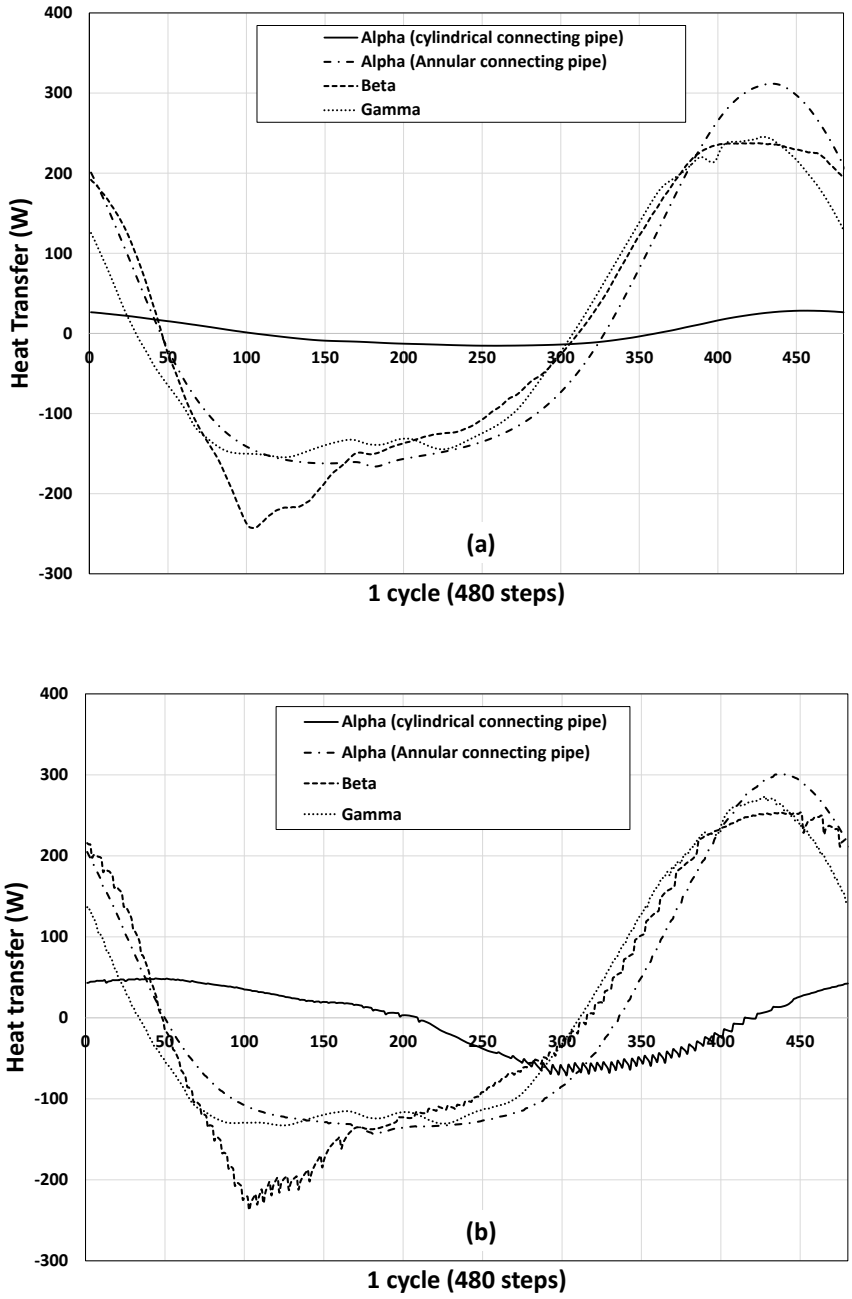

Figure 4.21 Heat transfer profiles in (a) narrow connecting pipe (b) total surface area.

CHAPTER 5

CONCLUSIONS & RECOMMENDATIONS

5.1 Conclusions

In this work a CFD simulation of laminar flow inside Stirling engine was performed. The performance of Stirling engine was optimized for different operational parameters. These parameters included the charge pressure (ranged from 1 to 4.5 bar), temperature boundary conditions (ranged from 300 K to 1300 K), and different working fluids (Air, He, and H_2). Then the radiative heat transfer was included in the analysis and its impact on Stirling engine performance was investigated. Moreover, the Stirling engine performance was analyzed for different fin shapes, different piston motion mechanisms, and different engine types. The main remarkable results of this work are:

- The optimum charge pressure which yields the most power output varies depending on the gas used. For beta-type Stirling engine with temperature limits of 300-800 K, the optimum charge pressures are 1.75 bar (for air), 2.5 bar (for He) and 10 bar (for H_2).
- For H_2 and He gasses, it is preferred to run Stirling engine at a pressure less than the optimum charge pressure for power output. Accordingly, the thermal efficiency will be improved. In return, a small amount of power output would be lost.

- At atmospheric charge pressure with a temperature limits difference (ΔT) greater than 700 K, it is recommended to use He gas to operate the Stirling engine because it provides high efficiency and power output. While at low temperature difference H_2 gas generates more power output than He gas, but the He gas has greater efficiency.
- Shifting the operational temperature range to high level leads to an increase in the power output, but it has a negative impact on thermal efficiency.
- For air and He gasses the power output increases proportionally with temperature differences between T_H and T_C. While for H_2 gas the relation is proportional up to ΔT equal to 700 K after which it shows reverse impacts.
- Ignoring radiative heat transfer results in underestimation of the power output and the thermal efficiency.
- The proposed fin shapes have a negative impact on the performance of Stirling engine because the working fluid is not circulating through the fins.
- Rhombic mechanism recorded the best power output (9.6 W) and thermal efficiency (8.29 %) compared to crankshaft and scotch mechanisms.
- Among the Stirling engine configurations, modified alpha-type (with annular connecting pipe) has the best power output and thermal efficiency (10.08%). Then it followed by gamma-type with power output and efficiency of 9.4W and 9.93%.

5.2 Recommendations and Future Work

An enormous effort was done in this study to achieve the research objectives. However, there is always a room for improvement. Therefore, further improvement in the performance of Stirling engine can be achieved by:

- Including the regenerator parts in Stirling engine modeling in order to enhance the performance of Stirling engine.
- Extend the parametric study of charge pressure to include different temperature boundary limits since in the current study the charge pressure optimization is done for temperature limits of 300 – 800 K.
- Investigate the performance of Stirling engine with more piston motion mechanisms such as lever controller and yoke mechanism.
- Extend the work to include the turbulent flow, so that further improvement in heat transfer can be accomplished.

References

[1] "International Energy Outlook 2016-World energy demand and economic outlook - Energy Information Administration." [Online]. Available: https://www.eia.gov/outlooks/ieo/world.cfm. [Accessed: 16-Jan-2017].

[2] V. C. S, *STRILING ENGINES: A BEGINNERS GUIDE*. 2011.

[3] "The Stirling Cycle Engine - Amazing Men and their Magical Machines." [Online]. Available: http://magicalmachines.weebly.com/the-stirling-cycle-engine.html. [Accessed: 16-Jan-2017].

[4] N. C. J. Chen and F. P. Griffin, "A review of Stirling engine mathematical models," 1998.

[5] R. W. Dyson, S. D. Wilson, and R. C. Tew, "Review of Computational Stirling Analysis Methods," no. October, 2004.

[6] C. Çinar and H. Karabulut, "Manufacturing and testing of a gamma type Stirling engine," *Renew. Energy*, vol. 30, no. 1, pp. 57–66, Jan. 2005.

[7] C. Cinar, S. Yucesu, T. Topgul, and M. Okur, "Beta-type Stirling engine operating at atmospheric pressure," *Appl. Energy*, vol. 81, no. 4, pp. 351–357, Aug. 2005.

[8] H. Karabulut, H. S. Yücesu, and C. Çinar, "Nodal analysis of a Stirling engine with concentric piston and displacer," *Renew. Energy*, vol. 31, no. 13, pp. 2188–2197, Oct. 2006.

[9] N. Jiang and T. W. Simon, "Heat Transfer and Fluid Dynamics Measurements in the Expansion Space of a Stirling Cycle Engine," no. December, 2006.

[10] K. Mahkamov, "Design Improvements to a Biomass Stirling Engine Using Mathematical Analysis and 3D CFD Modeling," vol. 128, no. September 2006, 2006.

[11] B. Kongtragool and S. Wongwises, "Performance of a twin power piston low temperature differential Stirling engine powered by a solar simulator," vol. 81, pp. 884–895, 2007.

[12] I. T. Ã, Y. Timoumi, and S. Ben Nasrallah, "Analysis and design consideration of mean temperature differential Stirling engine for solar application," vol. 33, pp. 1911–1921, 2008.

[13] Y. T. Ã, I. Tlili, and S. Ben Nasrallah, "Design and performance optimization of GPU-3 Stirling engines," vol. 33, pp. 1100–1114, 2008.

[14] Y. T. Ã, I. Tlili, and S. Ben Nasrallah, "Performance optimization of Stirling engines," vol. 33, pp. 2134–2144, 2008.

[15] L. S. Ã, P. Valdez, and J. Baro, “Design and construction of a Stirling engine prototype,” vol. 33, pp. 3506–3510, 2008.

[16] I. Batmaz, “Design and manufacturing of a V-type Stirling engine with double heaters,” vol. 85, pp. 1041–1049, 2008.

[17] N. Parlak, A. Wagner, M. Elsner, and H. S. Soyhan, “Thermodynamic analysis of a gamma type Stirling engine in non-ideal adiabatic conditions,” vol. 34, pp. 266–273, 2009.

[18] H. Karabulut and F. Aksoy, “Thermodynamic analysis of a b type Stirling engine with a displacer driving mechanism by means of a lever,” vol. 34, pp. 202–208, 2009.

[19] H. Karabulut, H. Serdar, C. Çınar, and F. Aksoy, “An experimental study on the development of a b -type Stirling engine for low and moderate temperature heat sources,” vol. 86, pp. 68–73, 2009.

[20] H. S. Yu, “Torque and power characteristics of a helium charged Stirling engine with a lever controlled displacer driving mechanism,” vol. l, pp. 138–143, 2010.

[21] C. Cheng and Y. Yu, “Numerical model for predicting thermodynamic cycle and thermal efficiency of a beta-type Stirling engine with rhombic-drive mechanism,” *Renew. Energy*, vol. 35, no. 11, pp. 2590–2601, 2010.

[22] A. A. El-ehwany, G. M. Hennes, E. I. Eid, and E. El-kenany, “Experimental investigation of the performance of an elbow-bend type heat exchanger with a water tube bank used as a heater or cooler in alpha-type Stirling machines,” *Renew. Energy*, vol. 36, no. 2, pp. 488–497, 2011.

[23] P. Puech and V. Tishkova, “Thermodynamic analysis of a Stirling engine including regenerator dead volume,” *Renew. Energy*, vol. 36, no. 2, pp. 872–878, 2011.

[24] C. Cheng and Y. Yu, “Dynamic simulation of a beta-type Stirling engine with cam-drive mechanism via the combination of the thermodynamic and dynamic models,” *Renew. Energy*, vol. 36, no. 2, pp. 714–725, 2011.

[25] C. Cheng and Y. Yu, “Combining dynamic and thermodynamic models for dynamic simulation of a beta-type Stirling engine with rhombic-drive mechanism,” *Renew. Energy*, vol. 37, no. 1, pp. 161–173, 2012.

[26] C. Cheng and H. Yang, “Optimization of geometrical parameters for Stirling engines based on theoretical analysis,” *Appl. Energy*, vol. 92, pp. 395–405, 2012.

[27] W. Chen, K. Wong, and L. Po, “A numerical analysis on the performance of a pressurized twin power piston gamma-type Stirling engine,” *Energy Convers. Manag.*, vol. 62, pp. 84–92, 2012.

[28] M. Ibrahim, “2-D CFD SIMULATION OF THE HEAT TRANSFER AND FLUID

DYNAMICS IN AN EXPERIMENTAL MODEL OF THE HOT END OF A STIRLING ENGINE," *Energytech*, pp. 1–11, 2012.

[29] S. C. Costa, H. Barrutia, J. Ander, and M. Tutar, "Numerical study of the pressure drop phenomena in wound woven wire matrix of a Stirling regenerator," *Energy Convers. Manag.*, vol. 67, pp. 57–65, 2013.

[30] Z. Li, Y. Haramura, Y. Kato, and D. Tang, "Analysis of a high performance model Stirling engine with compact porous-sheets heat exchangers," *Energy*, vol. 64, pp. 31–43, 2014.

[31] J. a. Araoz, M. Salomon, L. Alejo, and T. H. Fransson, "Non-ideal Stirling engine thermodynamic model suitable for the integration into overall energy systems," *Appl. Therm. Eng.*, vol. 73, no. 1, pp. 203–219, 2014.

[32] J. Bouvenot, B. Andlauer, P. Stabat, D. Marchio, B. Flament, B. Latour, and M. Siroux, "Gas Stirling engine uCHP boiler experimental data driven model for building energy simulation," *Energy Build.*, vol. 84, pp. 117–131, 2014.

[33] W.-L. Chen, K.-L. Wong, and Y.-F. Chang, "A computational fluid dynamics study on the heat transfer characteristics of the working cycle of a low-temperature-differential γ-type Stirling engine," *Int. J. Heat Mass Transf.*, vol. 75, pp. 145–155, Aug. 2014.

[34] S. Alfarawi, M. Webb-martin, S. Mahmoud, and R. K. Al-dadah, "Thermal Analysis of Stirling Engine to Power Automotive Alternator Using Heat from Exhaust Gases," *Energy Procedia*, vol. 61, pp. 2395–2398, 2014.

[35] S. Costa, M. Tutar, I. Barreno, and J. Esnaola, "Experimental and numerical flow investigation of Stirling engine regenerator," vol. 72, pp. 800–812, 2014.

[36] S. C. Costa, I. Barreno, M. Tutar, J. A. Esnaola, and H. Barrutia, "The thermal non-equilibrium porous media modelling for CFD study of woven wire matrix of a Stirling regenerator," *Energy Convers. Manag.*, vol. 89, pp. 473–483, 2015.

[37] C. J. Paul and A. Engeda, "Modeling a complete Stirling engine," *Energy*, vol. 80, pp. 85–97, 2015.

[38] H. Hosseinzade and H. Sayyaadi, "CAFS : The Combined Adiabatic – Finite Speed thermal model for simulation and optimization of Stirling engines," *Energy Convers. Manag.*, vol. 91, pp. 32–53, 2015.

[39] W. Chen, K. Wong, and Y. Chang, "A numerical study on the effects of moving regenerator to the performance of a beta-type Stirling engine," *HEAT MASS Transf.*, vol. 83, pp. 499–508, 2015.

[40] K. Makhkamov and D. B. Ingham, "Theoretical investigations on the Stirling engine working process," *Collect. Tech. Pap. 35th Intersoc. Energy Convers. Eng. Conf. Exhib. (Cat. No.00CH37022)*, vol. 1, 2000.

[41] K. Mahkamov, “An axisymmetric computational fluid dynamics approach to the analysis of the working process of a solar stirling engine.,” vol. 128, no. February, pp. 45–53, 2006.

[42] R. W. Dyson, S. D. Wilson, R. Tew, and R. Demko, “Fast Whole-Engine Stirling Analysis,” *October*, vol. 2005–5558, no. October, p. NASA/TM--2005--213960, 2005.

[43] C. Lin, X. Z. Wang, X. Chen, and Z. G. Zhang, “Improve the Free-Piston Stirling Engine Design with High Order Analysis Method,” *Appl. Mech. Mater.*, vol. 44–47, pp. 1991–1995, 2011.

[44] S. C. Costa, H. Barrutia, J. A. Esnaola, and M. Tutar, “Numerical study of the heat transfer in wound woven wire matrix of a Stirling regenerator,” *Energy Convers. Manag.*, vol. 79, pp. 255–264, 2014.

[45] Salazar, “A computational fluid dynamics study on the heat transfer characteristics of the working cycle of a β-type Stirling engine.” .

[46] E. Eid, “Performance of a beta-configuration heat engine having a regenerative displacer,” *Renew. Energy*, vol. 34, no. 11, pp. 2404–2413, 2009.

[47] E. Cardozo, C. Erlich, A. Malmquist, and L. Alejo, “Integration of a wood pellet burner and a Stirling engine to produce residential heat and power,” *Appl. Therm. Eng.*, vol. 73, no. 1, pp. 669–678, 2014.

[48] *ANSYS Fluent Theory Guide*, vol. 15317, no. November. 2013.

[49] F. Cverna, *Thermal properties of metals*. 2002.

Vitae

Name	:Ahmed Salih Hamza Abuelyamen
Nationality	:Sudanese
Date of Birth	:7/8/1990
Email	:ahmedsalih45@yahoo.com
Address	:Dhahran Blvd, KFUPM, Saudi Arabia

Academic Background:

- Master of Science in Mechanical Engineering, King Fahd University of Petroleum and Minerals, KSA (January 2017).
- Bachelor of Science in Mechanical Engineering, University of Khartoum, Sudan (October 2012).